

# Supporting Information

## Silver-Purine MOFs for High-Performance Multi-terminal Neuromorphic Memory

Subhra Jyoti Panda<sup>1</sup>, Kanha Ram Khator<sup>2</sup>, Priyanka Deswal<sup>3</sup>, Shashwat Nayak<sup>2</sup>, Durgesh Pandey<sup>4</sup>, Suraj K. Patel<sup>2</sup>, Suraj Kumar Agrawalla<sup>1</sup>, Dibyajyoti Ghosh<sup>4,5,\*</sup>, Satyaprasad P. Senanayak<sup>2,6,\*</sup>, Chandra Shekhar Purohit<sup>1,6,\*</sup>

<sup>1</sup>School of Chemical Sciences, National Institute of Science Education and Research (NISER),

An OCC of HBNI, Bhubaneswar, 752050, Odisha, India.

<sup>2</sup>Nanoelectronic and Device Physics Lab, School of Physical Sciences, National Institute of Science Education and Research (NISER), An OCC of HBNI, Bhubaneswar, 752050, Odisha, India.

<sup>3</sup>Department of Physics, Indian Institute of Technology, Delhi, Hauz Khas, New Delhi 110016, India.

<sup>4</sup>Department of Chemistry, Indian Institute of Technology, Delhi, Hauz Khas, New Delhi 110016, India.

<sup>5</sup>Department of Materials Science and Engineering Indian Institute of Technology, Delhi, Hauz Khas, New Delhi 110016, India

<sup>6</sup>Center for Interdisciplinary Sciences (CIS), National Institute of Science Education and Research (NISER), Bhubaneswar, Jatni, Khurda, Odisha 752050, India

E-mail: purohit@niser.ac.in, satyaprasad@niser.ac.in, dibyajyoti@iitd.ac.in

# Contents

1 Material and Methods .....	3
1.1 General Experimental:.....	3
1.2 Crystal Structure refinement detail: .....	3
1.3 Scanning electron microscopy (SEM):.....	3
1.4 High-resolution transmission electron microscopy (HR-TEM):.....	3
1.5 Experimental setup for optical illumination of the samples:.....	4
2 Chemical synthesis and characterization .....	4
2.1 Procedure for the synthesis of L-1: .....	4
2.2 Procedure for the synthesis of L-2: .....	6
2.3 Synthesis of Complex ACPSbF <sub>6</sub> :.....	8
2.4 Characterization of ACPSbF <sub>6</sub> .....	8
2.5 Synthesis of Complex ACPPF <sub>6</sub> :.....	11
2.6 Characterization of ACPPF <sub>6</sub> .....	11
2.7 Synthesis of Complex MCPSbF <sub>6</sub> : .....	14
2.8 Characterization of MCPSbF <sub>6</sub> .....	14
2.9 Synthesis of Complex MCPPF <sub>6</sub> : .....	17
2.10 Characterization of MCPPF <sub>6</sub> .....	17
2.11 Crystal structure of MCPNO <sub>3</sub> complex.....	18
2.12 Electron Microscopy Studies: .....	19
2.13 Table S1. Crystal data and structure refinement .....	21
2.14 Vrf entries in CIFs with level B errors .....	22
2.15 Calculation of anion density in each crystal:.....	22
3 Device fabrication and optimization of MCPSbF <sub>6</sub> .....	23
4 Scan rate dependence measurement .....	25
5 I-V Characteristics of the memristor device for varied channel lengths .....	27
6 Vacuum dependence measurement.....	28
7 Voltage dependence measurement .....	28
8 Ionic Conductivity measurement.....	30
9 Computational Methods.....	34
10 Structural Details .....	34
11 Stability of the memory devices under Biasing .....	37
12 Endurance of the memory device. ....	39
13 Heterosynaptic Plasticity of MCPSbF <sub>6</sub> neuromorphic devices .....	41

13.1 Heterosynaptic Plasticity Measurements: .....	41
13.2 Estimation of energy consumption in heterosynaptic plasticity:.....	42
14 Summary of memory and neuromorphic parameters for different devices .....	43
15 Hydrogen bond tables. ....	45
16 Reference: .....	46

## 1 Material and Methods

### 1.1 General Experimental:

All the chemicals were purchased from Sigma-Aldrich, SRL Chemicals, and Spectrochem and used without further purification. All the solvents were dry distilled before use according to the standard procedures. Nuclear magnetic resonance spectra ( $^1\text{H}$  NMR and  $^{13}\text{C}$  NMR) were recorded at Bruker AV-400 ( $^1\text{H}$  at 400 MHz and  $^{13}\text{C}$  at 100 MHz) spectrometers. NMR chemical shifts were referenced in parts per million (ppm) with respect to the residual solvent peak. Coupling constants are reported in Hz.

### 1.2 Crystal Structure refinement detail:

Single crystals of ACPSbF<sub>6</sub>, ACPPF<sub>6</sub>, MCPSbF<sub>6</sub>, and MCPPF<sub>6</sub> were coated with light paraffin oil and mounted on a SuperNova, Dual, Cu at home/near Pilatus 200K diffractometer at 100K cooled with liquid nitrogen. Using Olexsys software<sup>1</sup>, the structure was solved with the SHELXT<sup>2</sup> structure solution program using Intrinsic Phasing and refined with the SHELXL<sup>3</sup> refinement package using Least Squares minimization. Non-hydrogen atoms were refined anisotropically. Hydrogen atom positions were fixed at calculated positions. Molecules with the disorder were modeled by splitting the atoms, relating the occupancy with each splitted atom and ADP linking with each other. The constraints used in the crystal solving are EADP and DELU. The presence of heavy atoms (Ag, Sb) and the use of a copper anode lead to absorption issues. The large residual density near heavy atoms is due to the artifacts resulting from absorption correction. The CCDC numbers of the crystals are **2264862-2264865**.

### 1.3 Scanning electron microscopy (SEM):

Measurements were executed with a Merlin Compact field effect SEM (FESEM) with a GEMINI-I electron column, Zeiss Pvt. Ltd., Germany. Measurements were operated at 1.5-2 kV and WD of ~8.5 mm.

### 1.4 High-resolution transmission electron microscopy (HR-TEM):

Measurements were performed with a JEOL 2100F HRTEM, operated at 200 kV. The samples were prepared dry onto a copper lacey carbon grid (Sigma).

## 1.5 Experimental setup for optical illumination of the samples:

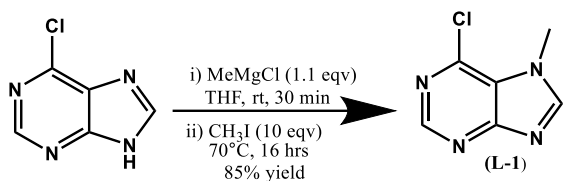
Exposing materials to light before the PXRD experiment for 18 hours. The white LED bulb used has 14 W and 1400 lm. The compound was kept under a petri dish, and water was on an upper petri dish to avoid heating.



## 2 Chemical synthesis and characterization

Both L-1 and L-2 were synthesized by following the reported procedure.<sup>4</sup>

### 2.1 Procedure for the synthesis of L-1:



To a 250 mL round bottom flask equipped with a magnetic stir bar, 2 g (12.94 mmol, 1 equiv.) of 6-chloro-9H-purine was added, and the flask was purged with N<sub>2</sub> several times after removal of air by high vacuum. 50 mL of THF was added to the RB, followed by 4.75 mL (14.234 mmol, 1.1 equiv.) of MeMgCl at 0°C. After 30 minutes, the ice bath was removed. Methyl Iodide (13 mL, 129.4 mmol, 10 equiv.) was added, and the reaction mixture was refluxed at 70°C for 16 hours. After this time, the TLC indicated the completion of the reaction. Methanol was added at room temperature to quench the reaction. The reaction mixture was evaporated under reduced pressure using a rotary evaporator, and the crude product was purified by column chromatography over silica

gel (230-400 mesh) using 2% MeOH in DCM. 1.85 g of pure product was obtained (85% yield).  $^1\text{H}$  NMR (400 MHz,  $\text{CD}_3\text{OD}$ )  $\delta$  (in ppm) = 8.75 (s, 1H), 8.59 (s, 1H), 4.18 (s, 3H);  $^{13}\text{C}$  NMR (100 MHz,  $\text{CD}_3\text{OD}$ )  $\delta$  (in ppm) = 162.44, 152.98, 152.28, 145.01, 124.5, 34.82

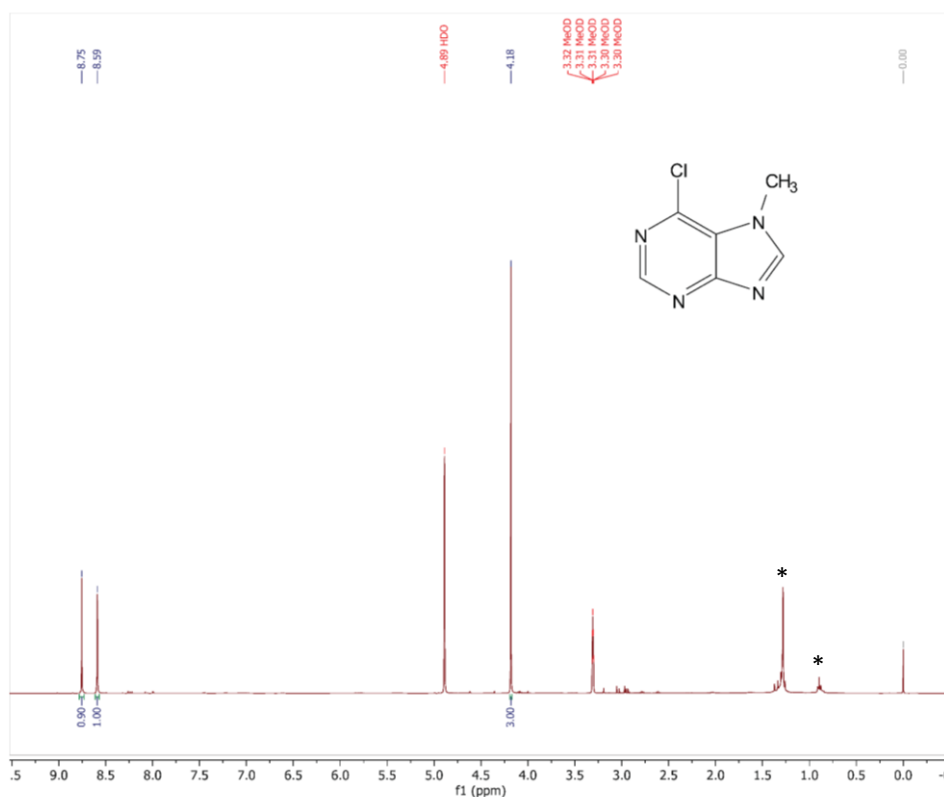


**Figure S1.**  $^1\text{H}$  NMR spectrum (400 MHz, 298K,  $\text{CD}_3\text{OD}$ ) of L1 (\* is the grease peak)<sup>5</sup>

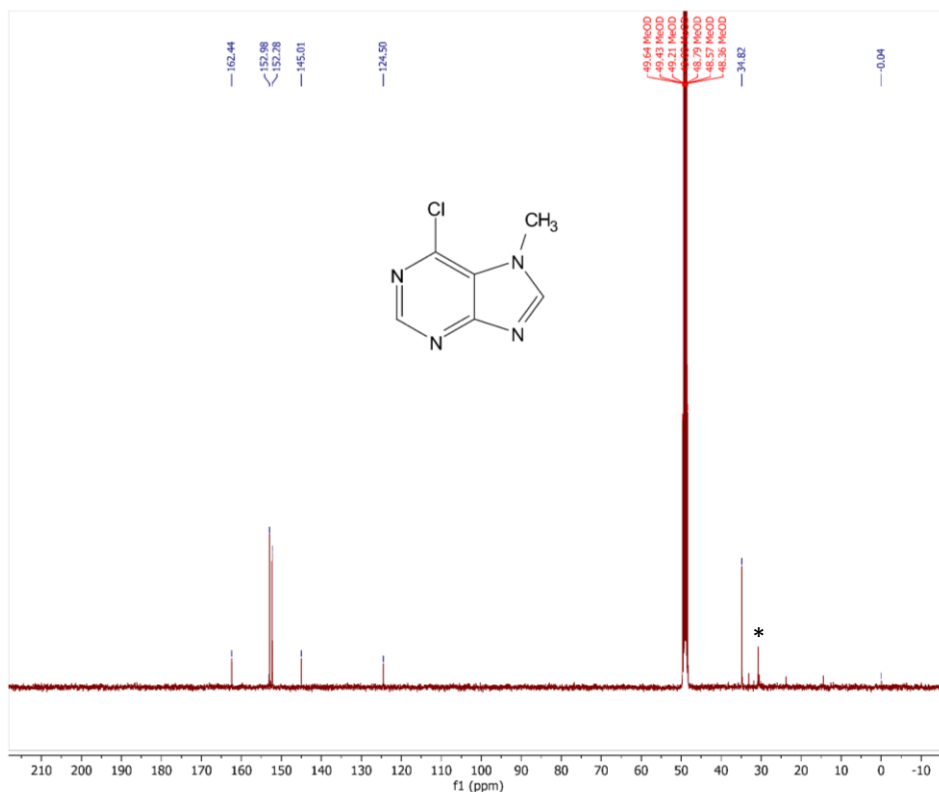
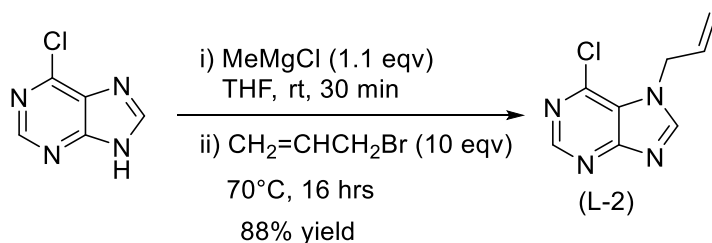


**Figure S2.**  $^{13}\text{C}$  NMR spectrum (100 MHz, 298K,  $\text{CD}_3\text{OD}$ ) of **L1** (\* is the grease peak)<sup>5</sup>

## 2.2 Procedure for the synthesis of L-2:



To a 250 mL round bottom flask equipped with a magnetic stir bar, 2g (12.94 mmol, 1 equiv.) of 6-chloro-9H-purine was added, and the flask was purged with  $\text{N}_2$  several times after removal of air by high vacuum. Later, 50 mL of THF was added to the RB, followed by the 4.75mL (14.234 mmol, 1.1 equiv.) of  $\text{MeMgCl}$  at 0°C. The reaction mixture was stirred at room temperature for 30 minutes. The allyl bromide 11.2 mL (129.4 mmol, 10 equiv.) was added, and the reaction was refluxed at 70°C for 16 hours. After this time, TLC indicated the completion of the reaction; methanol was added to quench the reaction at room temperature. The reaction mixture was evaporated under reduced pressure, and the crude reaction mixture was purified by column chromatography over silica gel (230-400 mesh) by 2% (MeOH/DCM). The pure product obtained was 2.2g (88% yield).  $^1\text{H}$  NMR (400 MHz,  $\text{CD}_3\text{OD}$ )  $\delta$  (in ppm) = 8.79 (s, 1H), 8.69 (s, 1H), 6.18 (m, 1H), 5.32 (d, 1H), 5.21 (m, 2H), 5.05(d, 1H);  $^{13}\text{C}$  NMR (101 MHz,  $\text{CD}_3\text{OD}$ )  $\delta$  (in ppm) = 161.2, 151.77, 150.44, 143.36, 132.98, 122.42, 117.28, 48.83

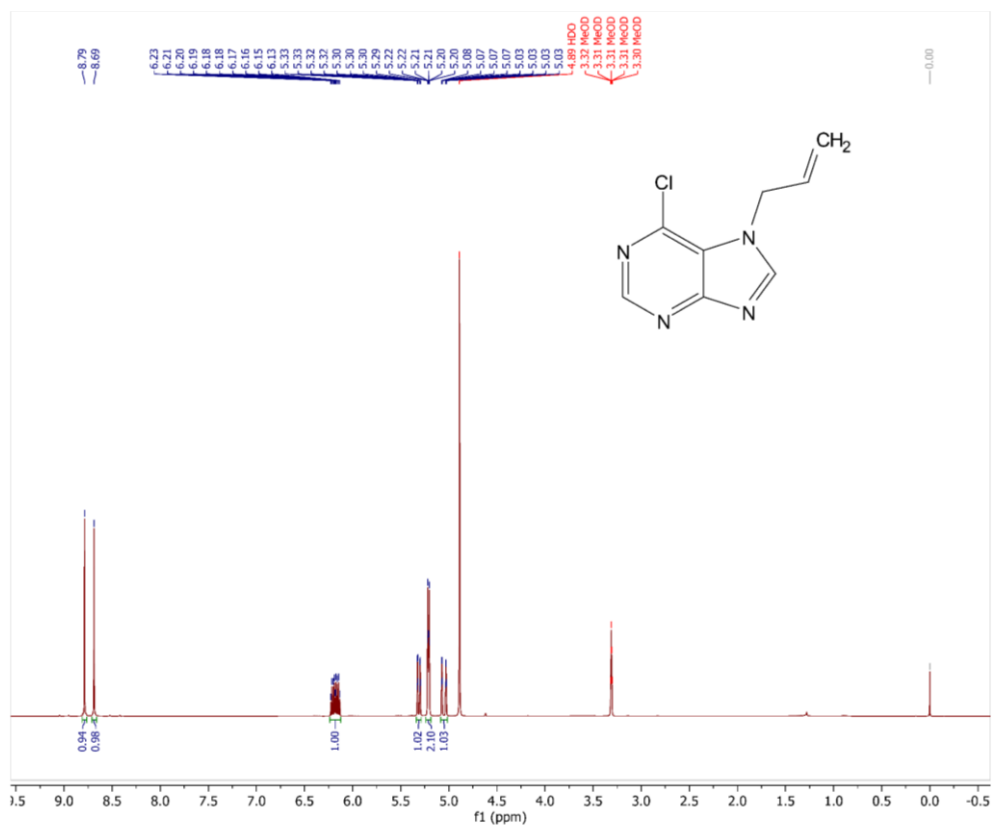


**Figure S3.** <sup>1</sup>H NMR spectrum (400 MHz, 298K, CD<sub>3</sub>OD) of L-2.

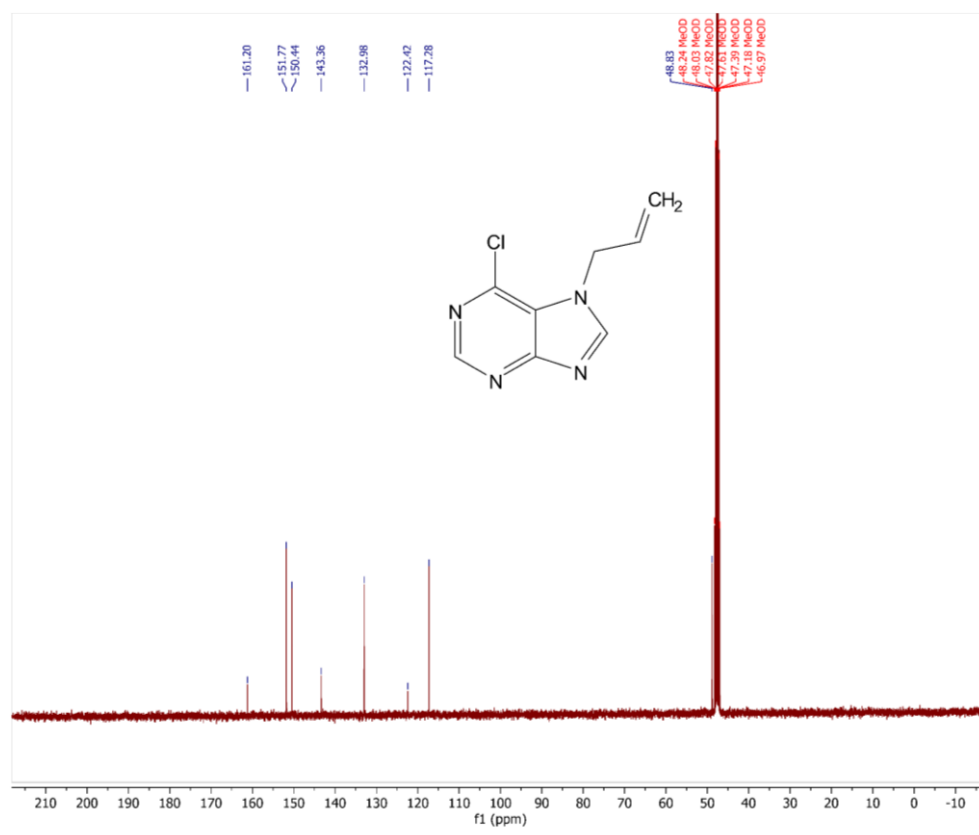


**Figure S4.** <sup>13</sup>C NMR spectrum (100 MHz, 298K, CD<sub>3</sub>OD) of L-2.

### 2.3 Synthesis of Complex ACPSbF<sub>6</sub>:

Ligand L-2 (15 mg, 0.077 mmol, 1 equiv.) was dissolved in methanol (2.5 mL) and was added to Silver hexafluoroantimonate(V) (17.6 mg, 0.115 mmol, 1.5 equiv.) solution in methanol (2.5 mL). The mixture was left for slow evaporation at room temperature in dark conditions. In 4 days, colorless needle-shaped crystals were obtained. These crystals were also found suitable for single crystal study. <sup>1</sup>H NMR (400 MHz, CD<sub>3</sub>OD) δ (in ppm) = 8.99 (s, 1H), 8.91 (s, 1H), 6.2 (m, 1H), 5.38 (d, 1H), 5.29 (m, 2H), 5.19 (d, 1H).

### 2.4 Characterization of ACPSbF<sub>6</sub>

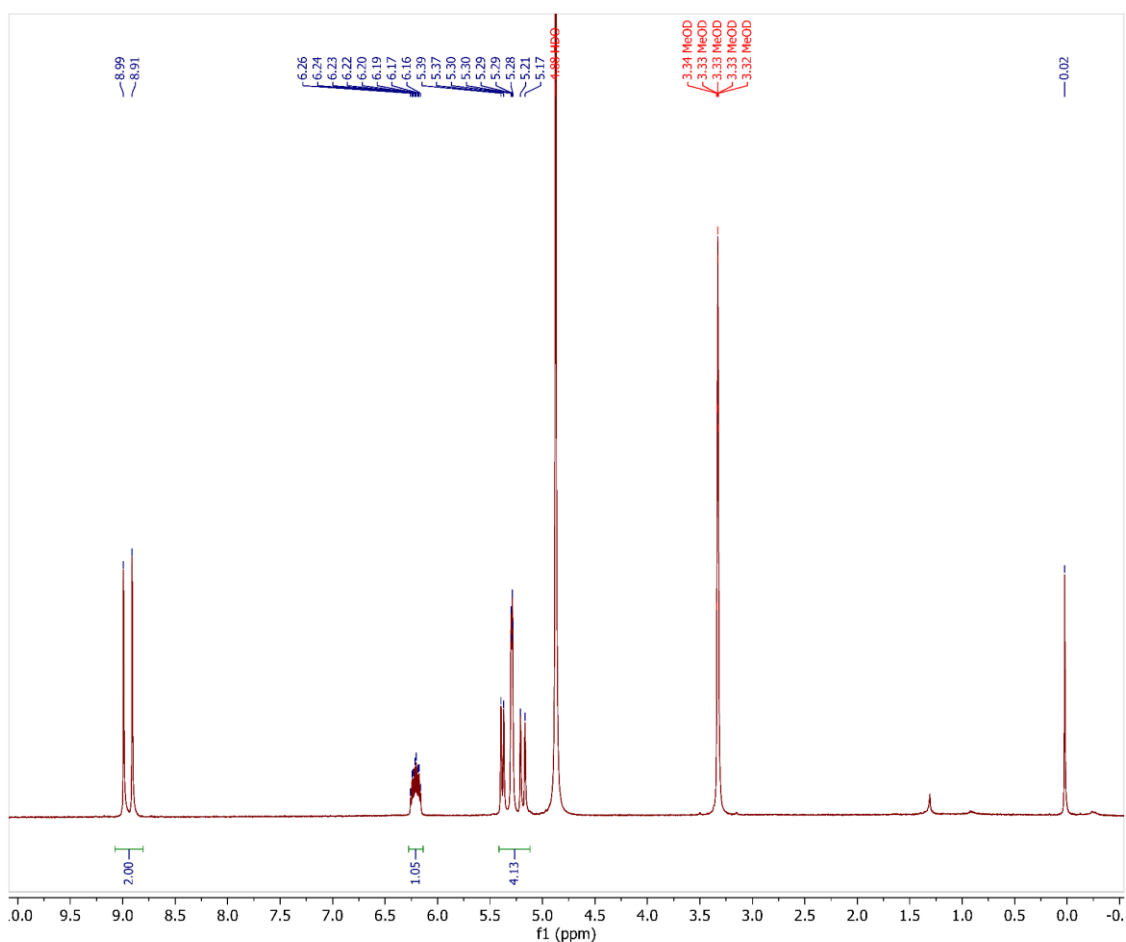


**Figure S5a.** <sup>1</sup>H NMR spectrum (400 MHz, 298K, CD<sub>3</sub>OD) of ACPSbF<sub>6</sub>.

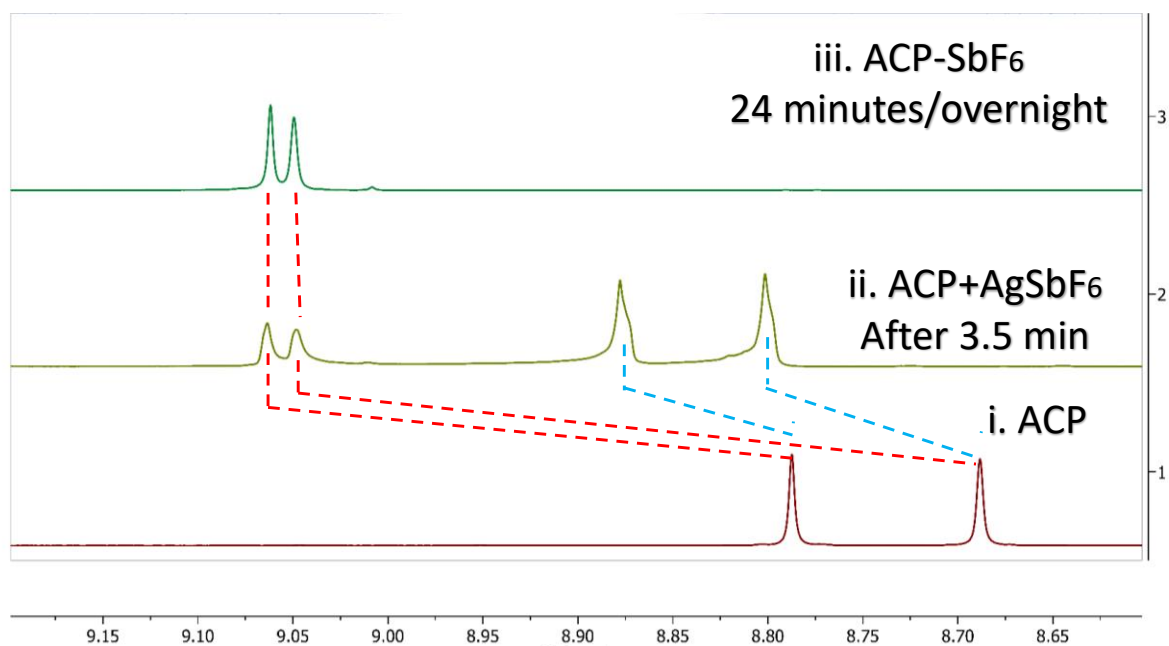


**Figure S5b.**  $^1\text{H}$  NMR kinetics study spectrum (400 MHz, 298K,  $\text{CD}_3\text{OD}$ ) of  $\text{ACPSbF}_6$ .

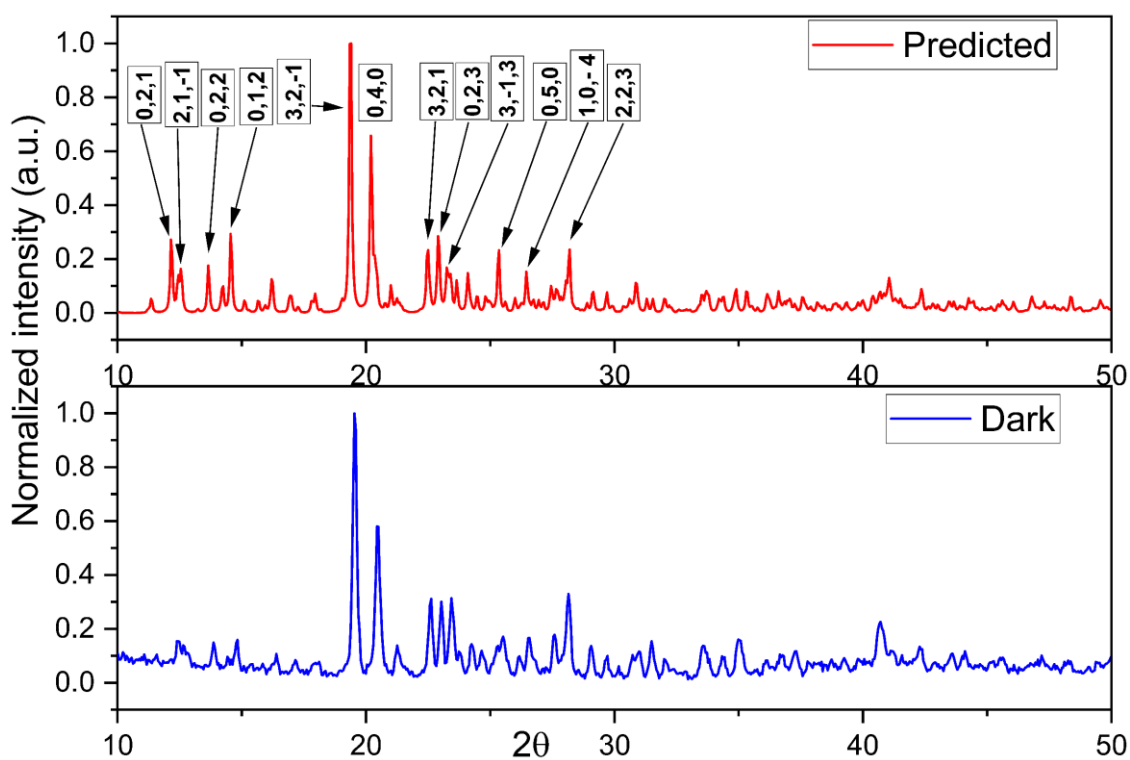


**Figure S6.** Simulated (upper, red) and Experimental in the dark (lower, blue) X-ray powder diffraction patterns of  $\text{ACPSbF}_6$ .

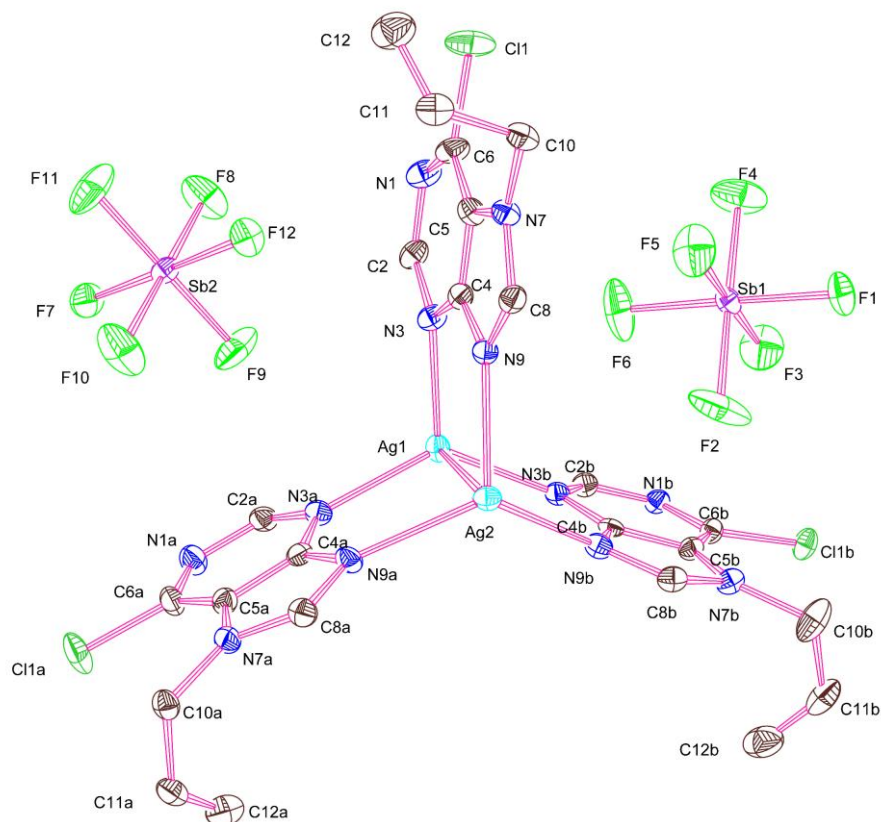


**Figure S7:** ORTEP diagram of ACPSbF<sub>6</sub> (50% probability)

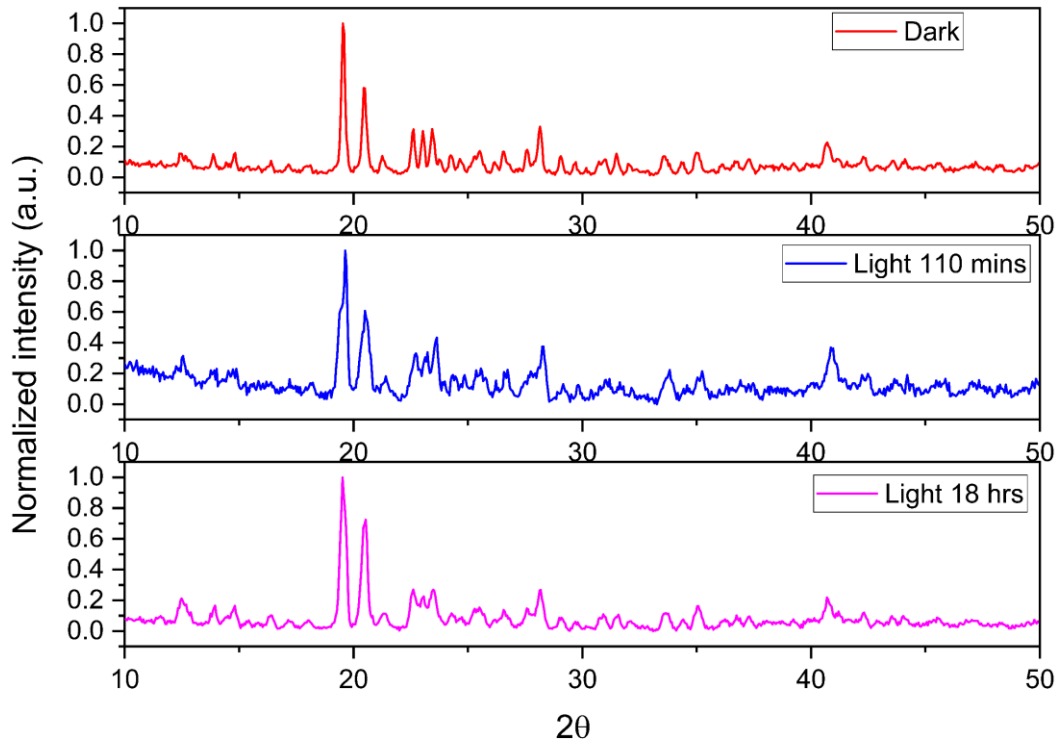


**Figure S8.** Experimental i) In dark (top, red) ii) exposed to light for 110 minutes (middle, blue) iii) exposed to light for 18 hours (bottom, pink) X-ray powder diffraction patterns of ACPSbF<sub>6</sub>. This shows the stability of the ACPSbF<sub>6</sub> when exposed to light though the presence of silver ions in the complex.

## 2.5 Synthesis of Complex ACPPF<sub>6</sub>:

Ligand L-2 (15 mg, 0.077 mmol, 1 equiv.) was dissolved in methanol (2 mL) and was added to Silver hexafluorophosphate (13 mg, 0.115 mmol, 1.5 equiv.) solution in methanol (2 mL). The mixture was left for slow evaporation at room temperature in dark conditions. In a week, colorless block-shaped crystals appeared. A suitable crystal without flaw was picked for a single crystal study. <sup>1</sup>H NMR (400 MHz, CD<sub>3</sub>OD) δ (in ppm) = 9.00 (s, 1H), 8.93 (s, 1H), 6.20 (m, 1H), 5.38 (d, 1H), 5.3 (m, 2H), 5.2 (d, 1H).

## 2.6 Characterization of ACPPF<sub>6</sub>

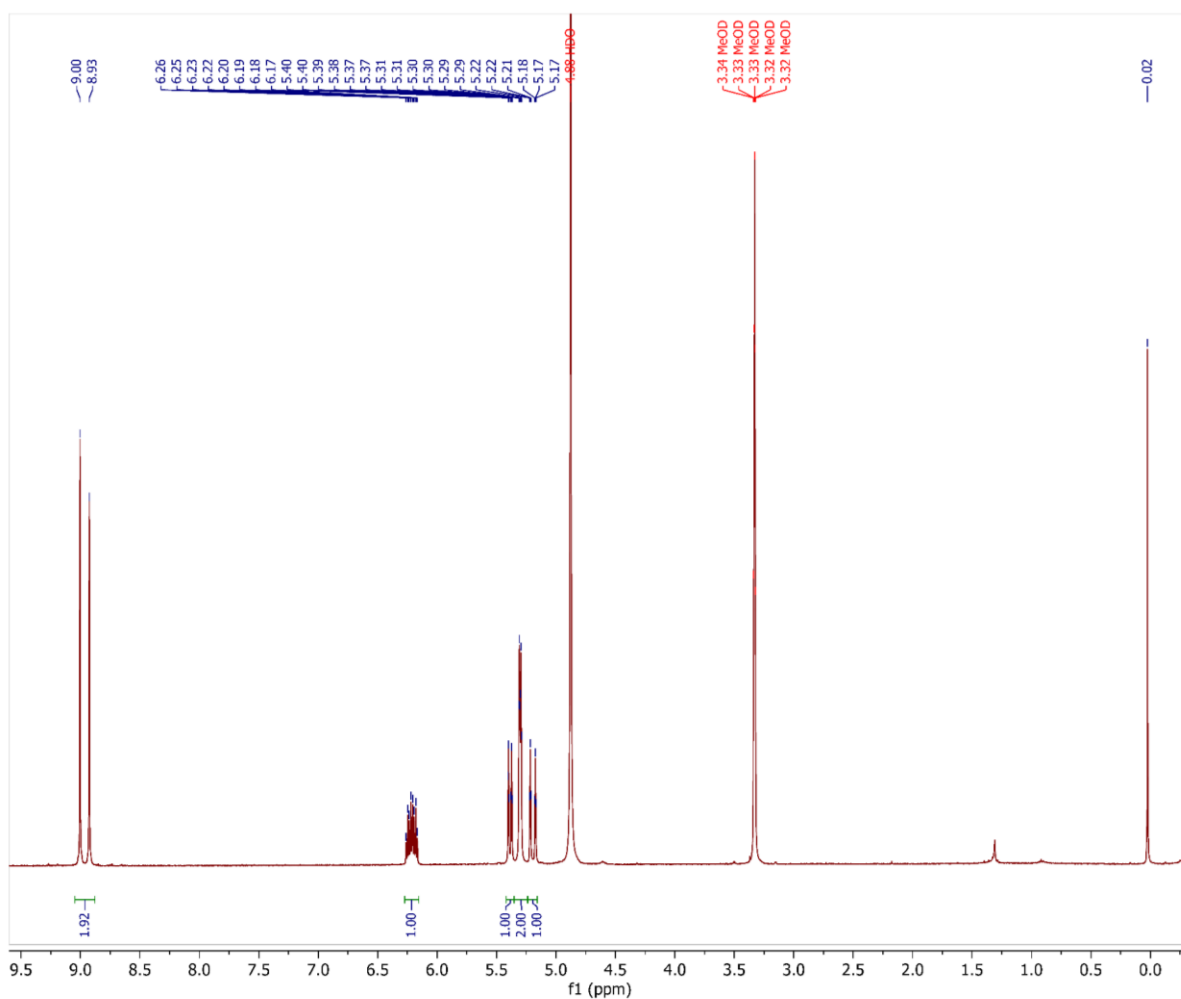


**Figure S9.** <sup>1</sup>H NMR spectrum (400 MHz, 298K, CD<sub>3</sub>OD) of ACPPF<sub>6</sub>.

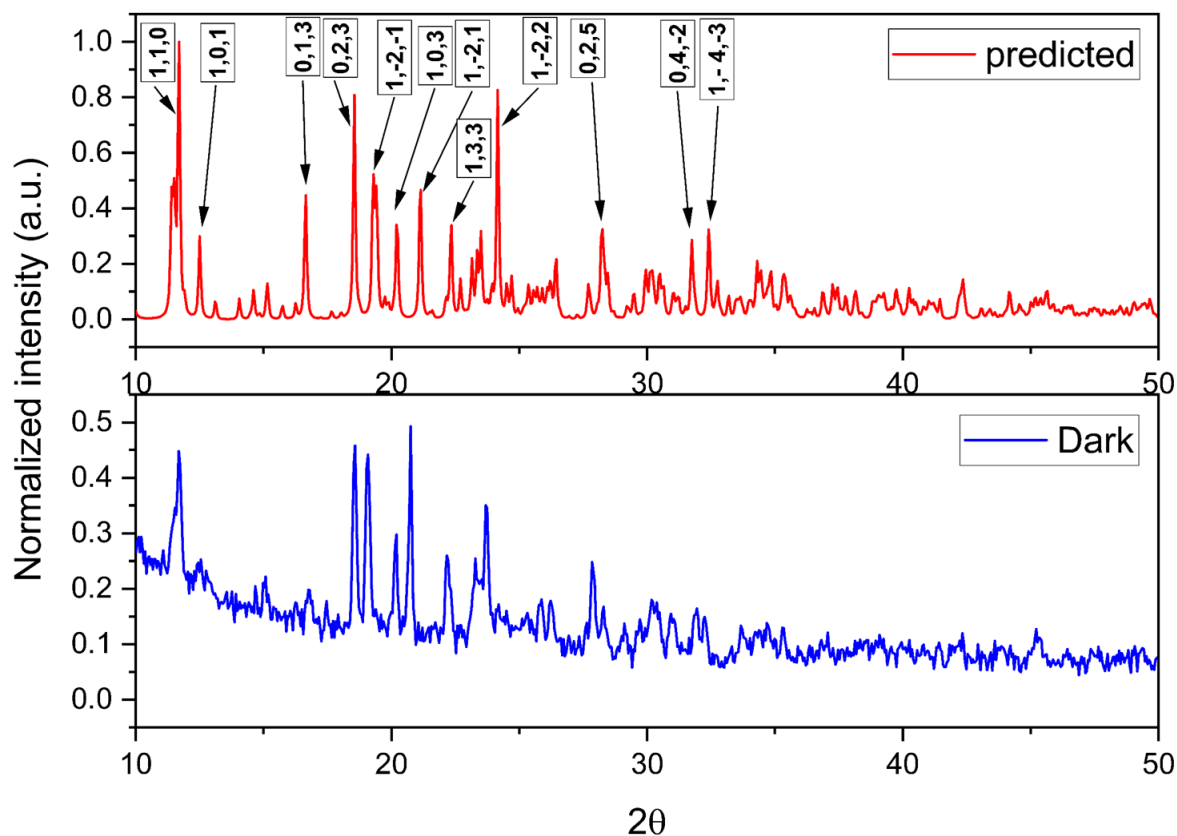


**Figure S10.** Simulated (upper, red) and Experimental in dark (lower, blue) X-ray powder diffraction patterns of **ACPPF<sub>6</sub>**.

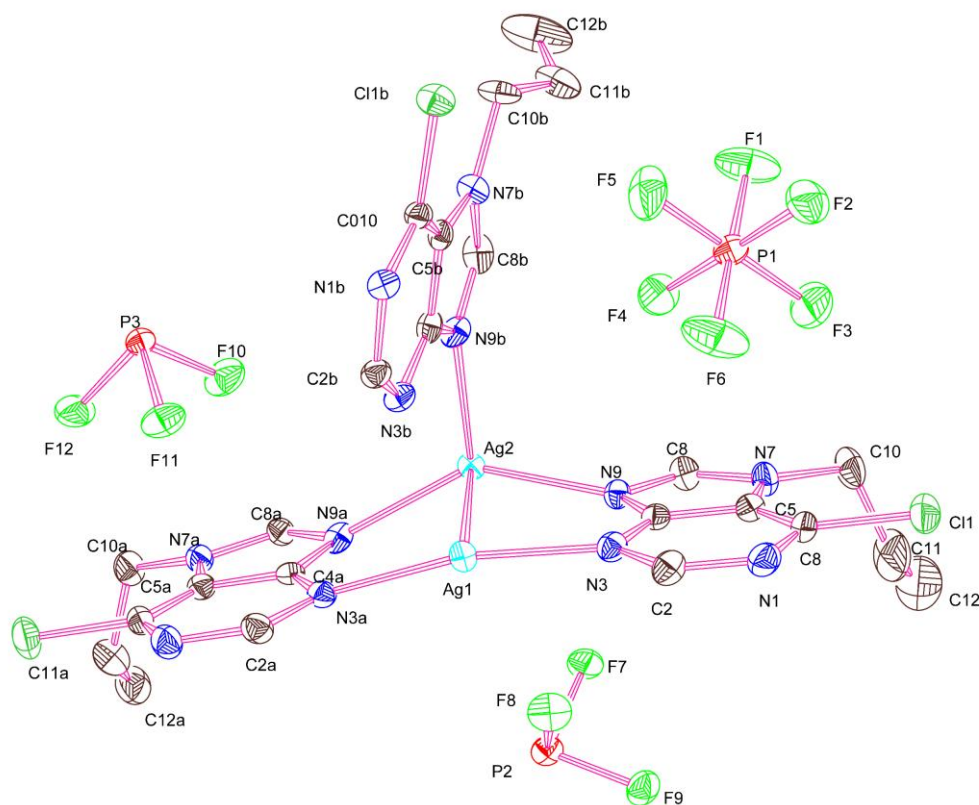


**Figure S11:** ORTEP diagram of **ACPPF<sub>6</sub>** (50% probability)

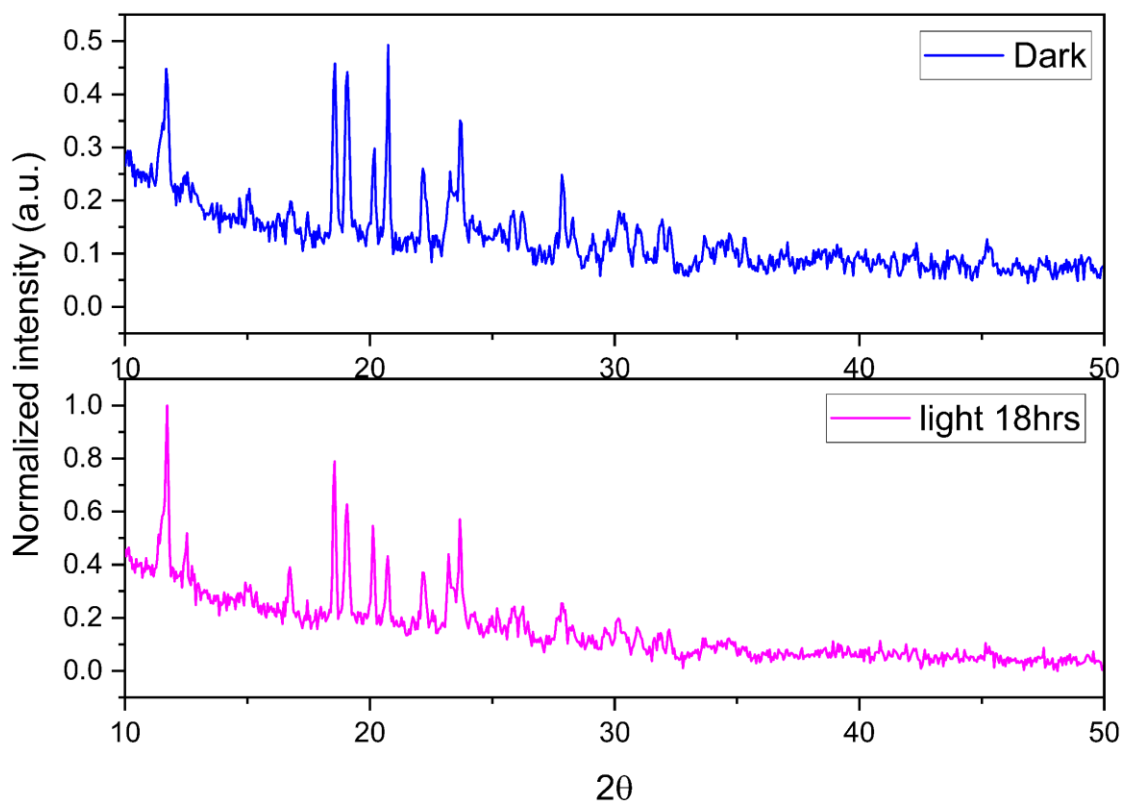


**Figure S12.** Experimental i) In dark (top, blue) ii) exposed to light for 18 hours (bottom, pink) X-ray powder diffraction patterns of **ACPPF<sub>6</sub>**. This shows the stability of the **ACPPF<sub>6</sub>** when exposed to light though the presence of silver ions in the complex.

## 2.7 Synthesis of Complex $\text{MCPSbF}_6$ :

Ligand L-1 (15 mg, 0.089 mmol, 1 equiv.) was dissolved in methanol (2 mL) and was added to Silver hexafluoroantimonate(V) (30.5 mg, 0.089 mmol, 1 equiv.) solution in methanol (2 mL). The mixture was left for slow evaporation at room temperature in dark conditions. After a week, colorless block-shaped crystals appeared suitable for single crystal study.

## 2.8 Characterization of $\text{MCPSbF}_6$

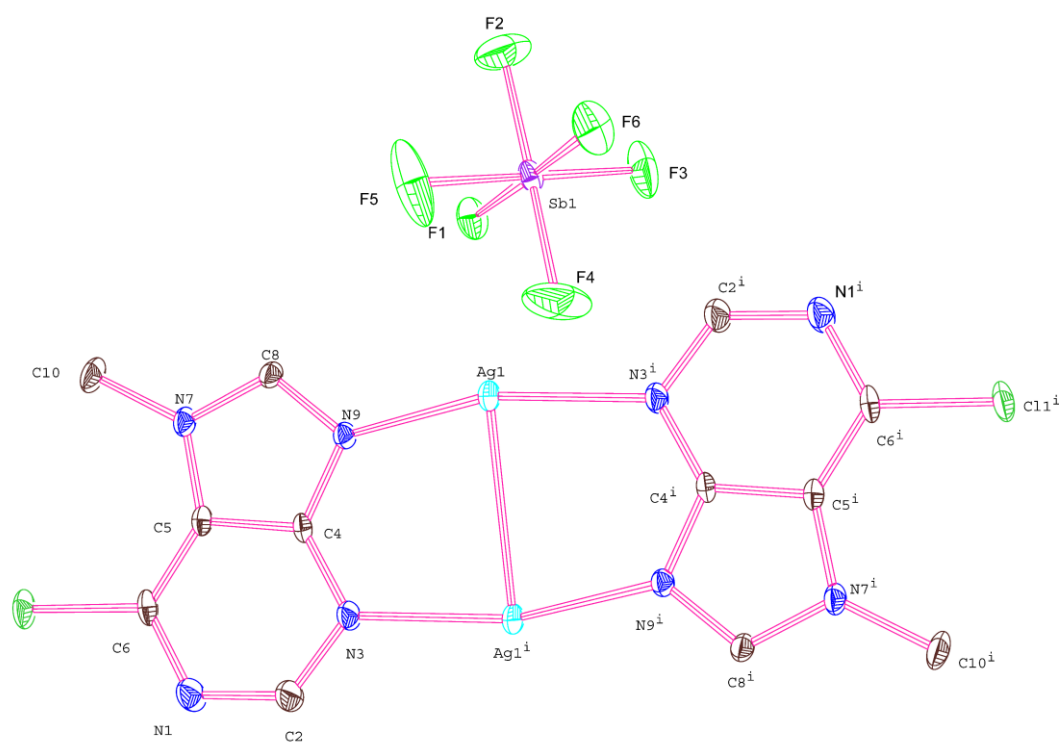


**Figure S13:** ORTEP diagram of  $\text{MCPSbF}_6$  (50% probability) symmetrically grown.

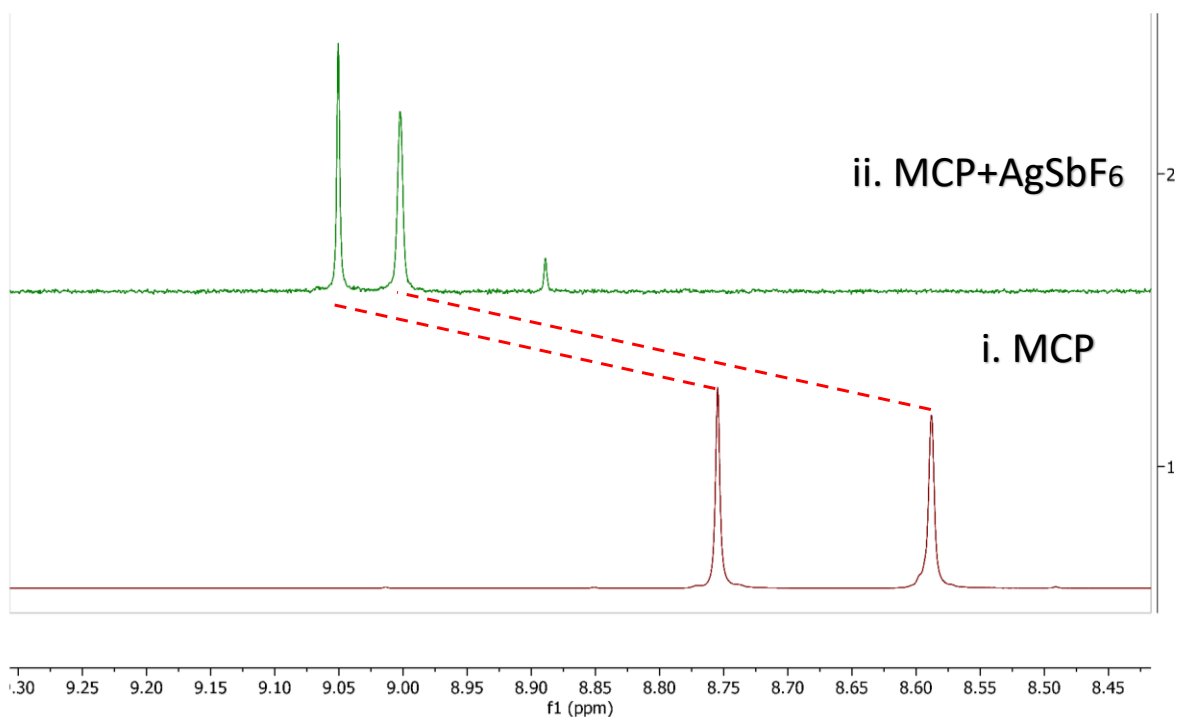


**Figure S14.**  $^1\text{H}$  NMR kinetics study spectrum (400 MHz, 298K,  $\text{CD}_3\text{OD}$ ) of  $\text{MCPSbF}_6$  (i)  $^1\text{H}$  NMR spectrum of two aromatic protons present in N7-methyl-6-chloropurine (MCP) (ii) The shift of the aromatic protons downfield upon metalation is observed in the  $^1\text{H}$  NMR of  $\text{MCPSbF}_6$ .

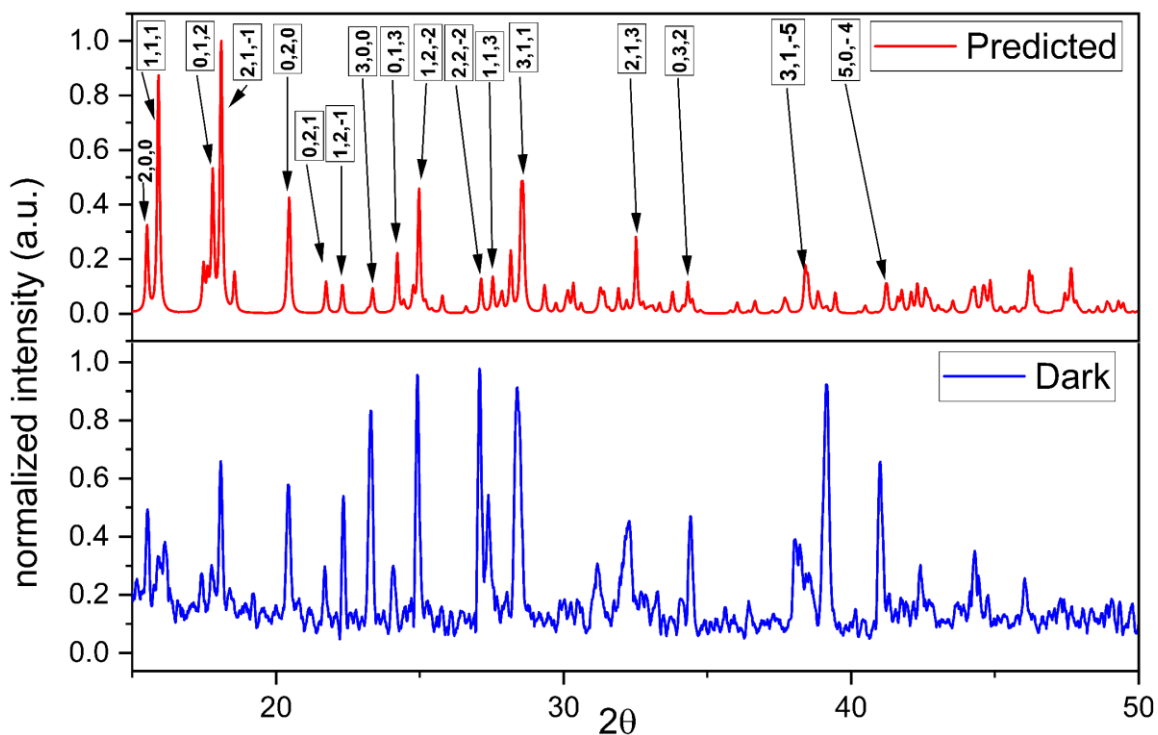


**Figure S15.** Simulated (upper, red) and Experimental in the dark (lower, blue) X-ray powder diffraction patterns of  $\text{MCPSbF}_6$ .

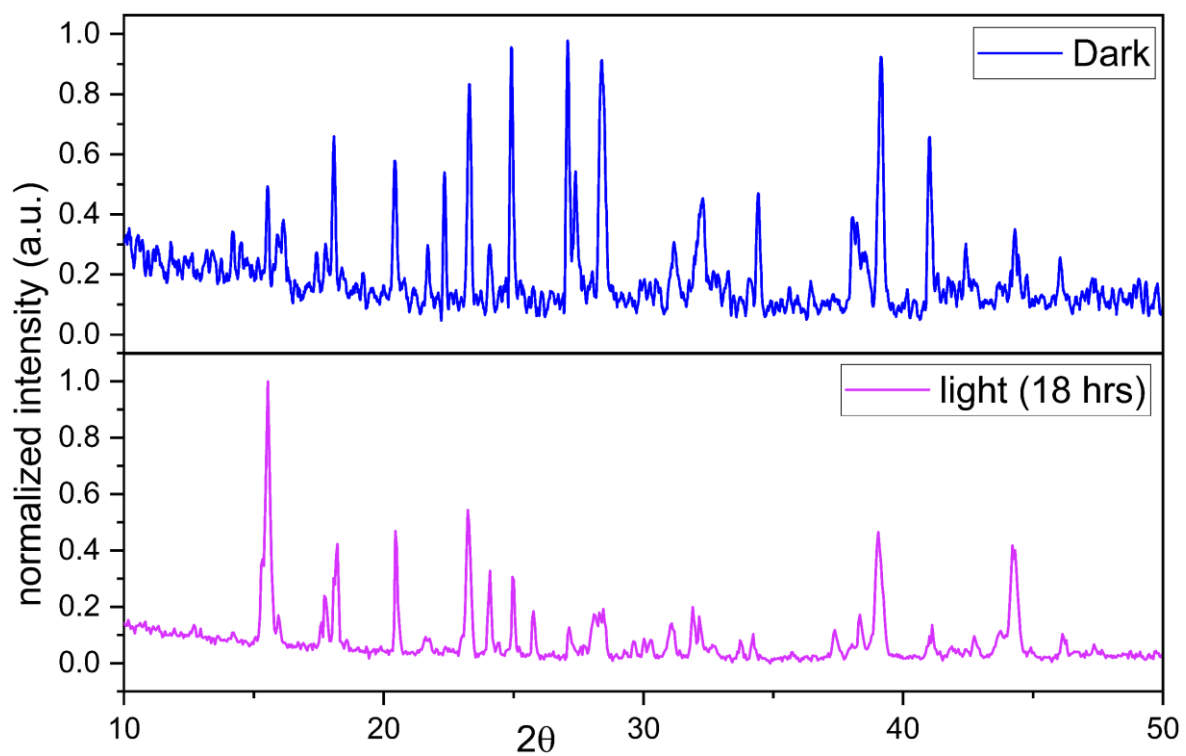


**Figure S16.** Experimental i) In dark (top, blue) ii) exposed to light for 18 hours (bottom, pink) X-ray powder diffraction patterns of **MCPSbF<sub>6</sub>**. This shows the stability of the MCPSbF<sub>6</sub> when exposed to light, though silver atoms are present.

## 2.9 Synthesis of Complex MCPPF<sub>6</sub>:

Ligand L-1 (15 mg, 0.089 mmol, 1 equiv.) was dissolved in methanol (2 mL) and was added to Silver hexafluorophosphate (22.5 mg, 0.089 mmol, 1 equiv.) solution in methanol (2 mL). The mixture was left for slow evaporation at room temperature in dark conditions. After 3 days, colorless block-shaped crystals appeared suitable for single crystal study.

## 2.10 Characterization of MCPPF<sub>6</sub>

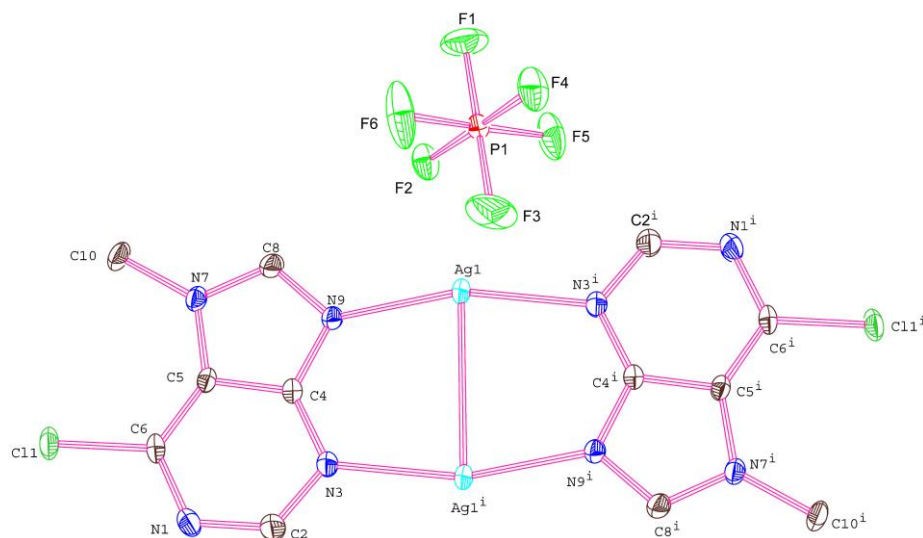


**Figure S17:** ORTEP diagram of MCPPF<sub>6</sub> (50% probability) symmetrically grown.

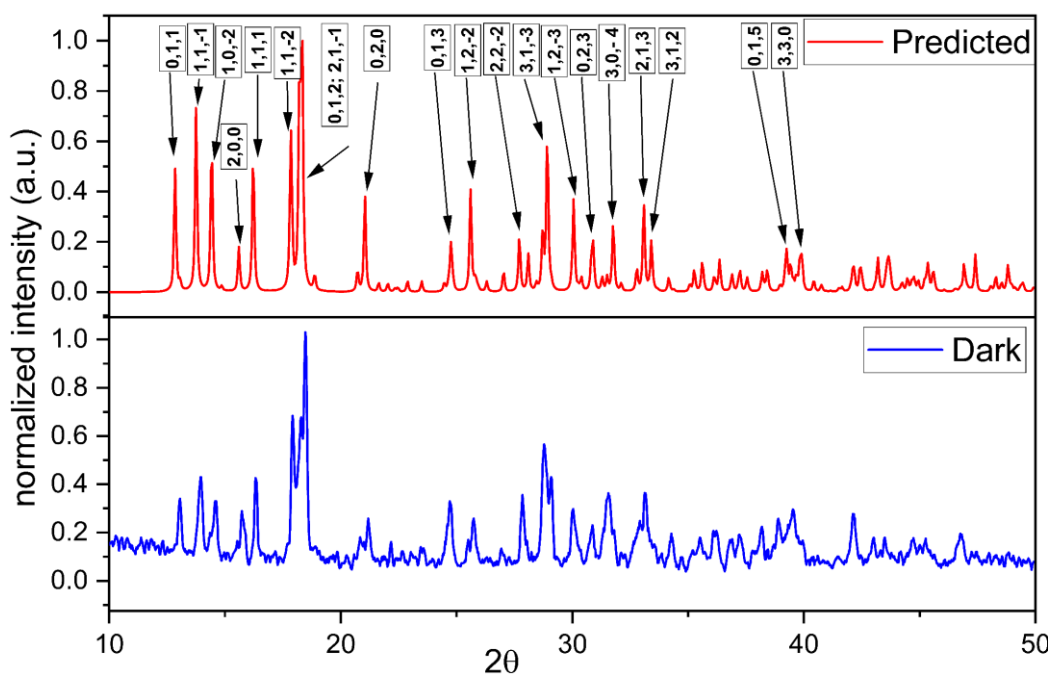


**Figure S18.** Simulated (upper, red) and Experimental in the dark (lower, blue) X-ray powder diffraction patterns of MCPPF<sub>6</sub>.

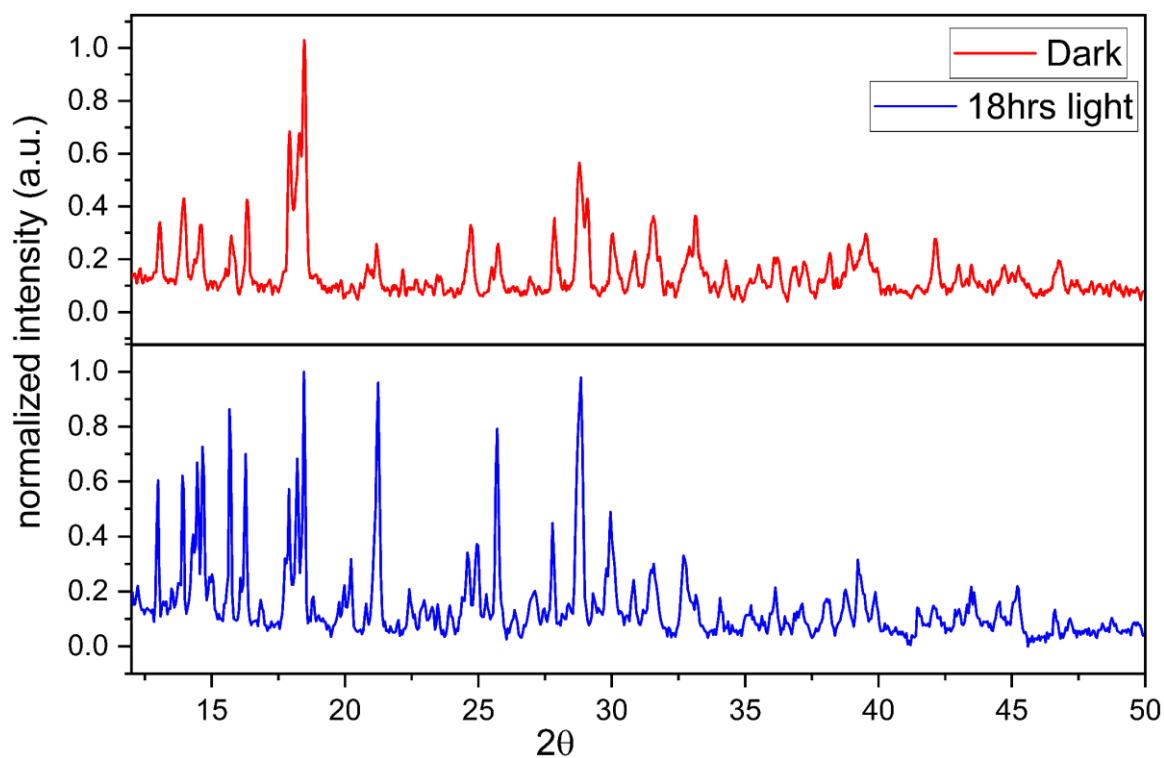


**Figure S19.** Experimental i) In dark (top, blue) ii) exposed to light for 18 hours (bottom, pink) X-ray powder diffraction patterns of **MCPPF<sub>6</sub>**. This shows the stability of the MCPPF<sub>6</sub> to light, though silver ions are present in the complex.

## 2.11 Crystal structure of MCPNO<sub>3</sub> complex

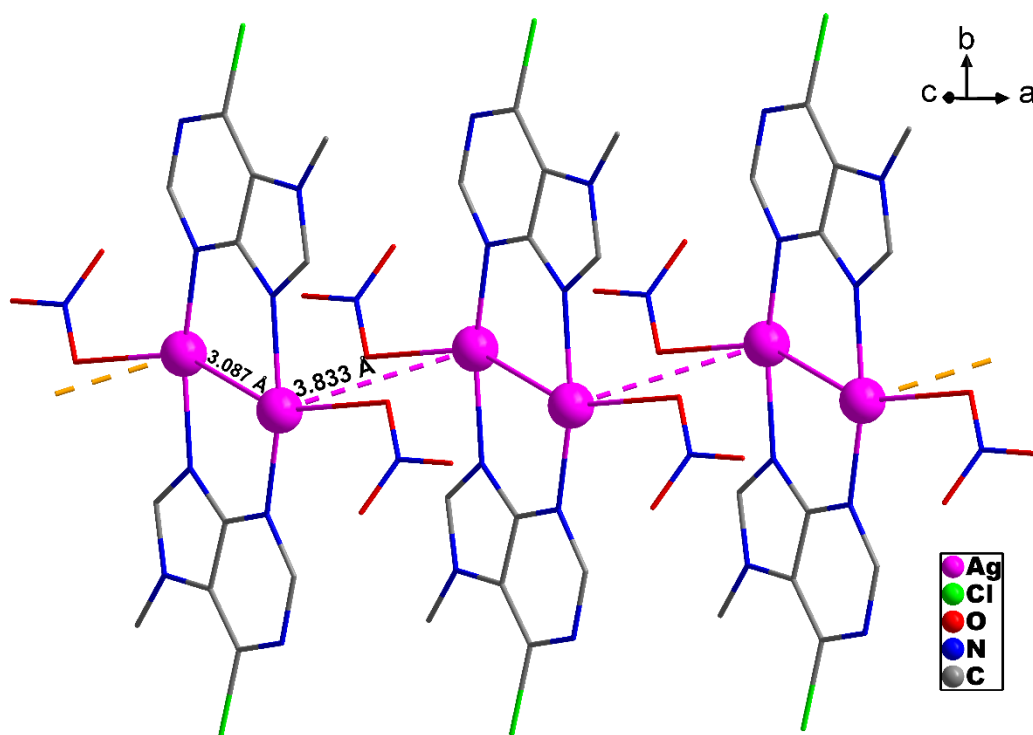


**Figure S20.** The molecular structure of **MCPNO<sub>3</sub>** in the wireframe model with Ag atom is in the ball model.

## 2.12 Electron Microscopy Studies:

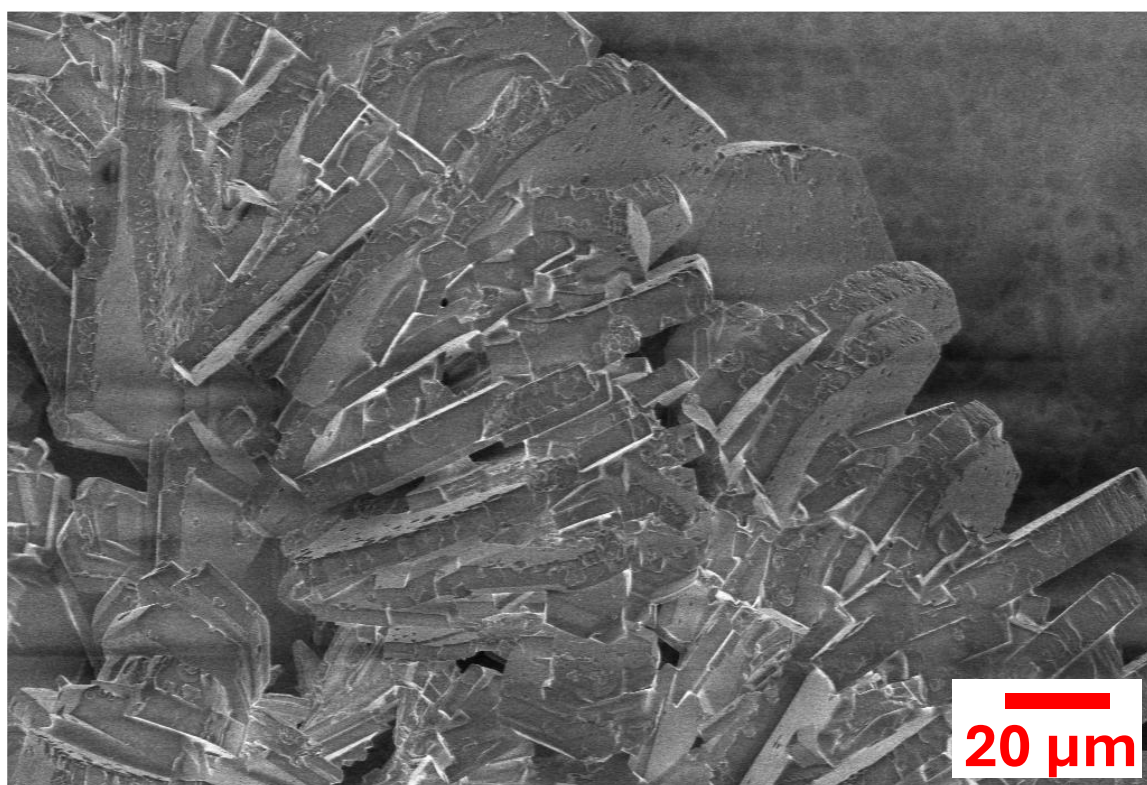


**Figure S21.** SEM image of MCPPF<sub>6</sub> MOF (multiple dropcast of 5.5 mg/mL solution was done).

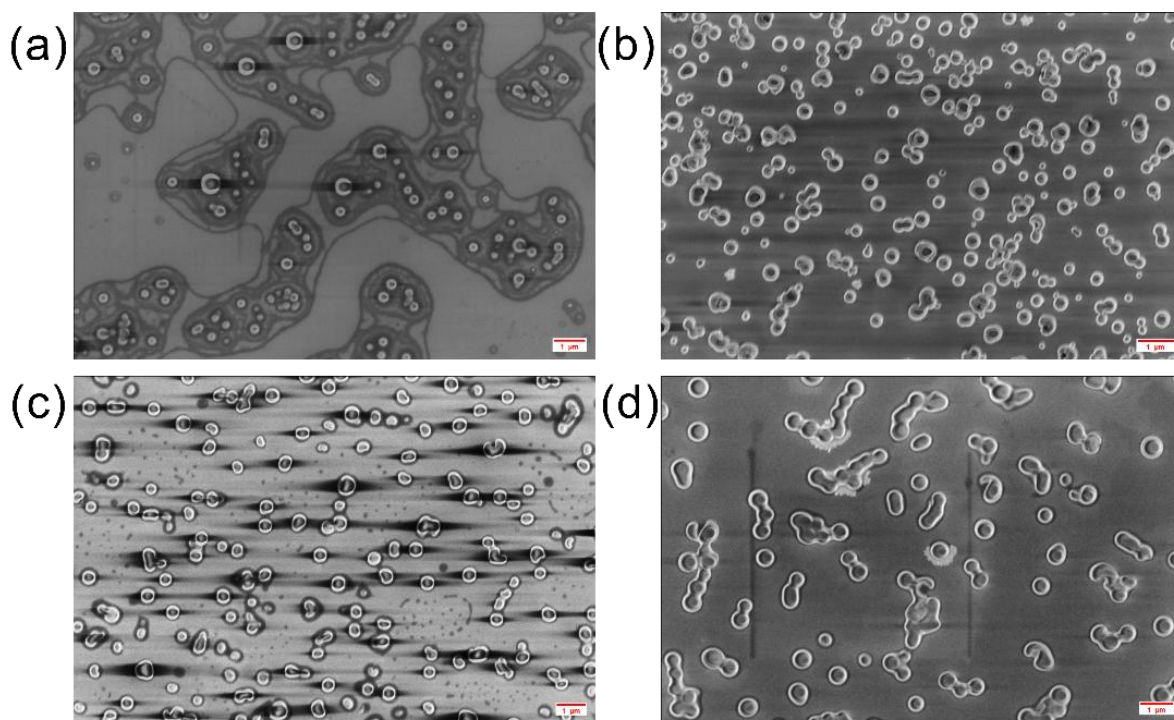


**Figure S22.** SEM image of MOFs in dilute concentration (a) ACPSbF<sub>6</sub> (b) MCPSbF<sub>6</sub> (c) ACPPF<sub>6</sub> (d) MCPPF<sub>6</sub>. (A single 10  $\mu$ L drop cast of 3 mg/mL solution was done)

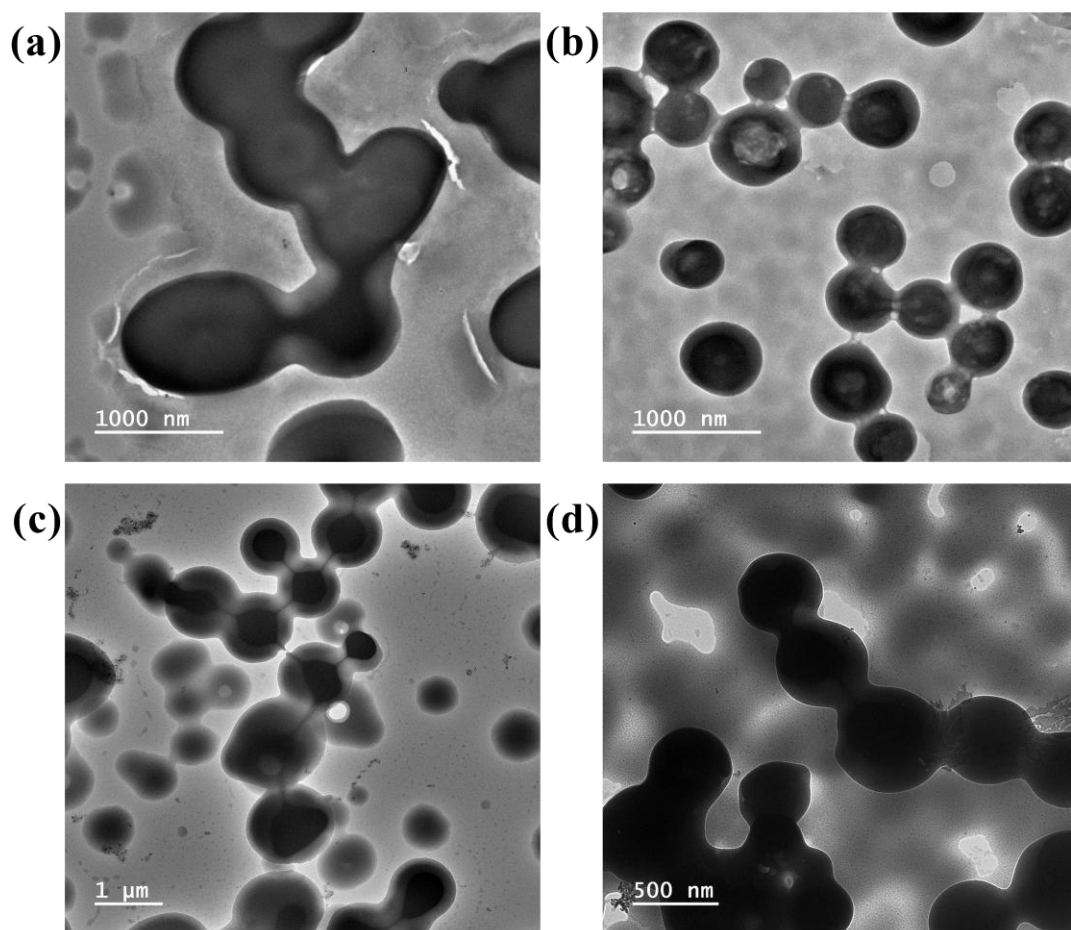


**Figure S23.** TEM image of MOFs (a) ACPSbF<sub>6</sub> (b) MCPSbF<sub>6</sub> (c) ACPPF<sub>6</sub> (d) MCPPF<sub>6</sub>. MOFs exhibited nano sphere-like morphology. (A single 3  $\mu$ L drop cast of 2 mg/mL solution was done)

## 2.13 Table S1. Crystal data and structure refinement

Identification code	SJP-DB-Sb ACPSbF <sub>6</sub> (MOF-1)	SJP-DB-PF ACPPF <sub>6</sub> (MOF- 2)	SJP-ME-Sb MCPSbF <sub>6</sub> (MOF-3)	SJP-PF-Me MCPPF <sub>6</sub> (MOF- 4)
CCDC Number	2264863	2264862	2264864	2264865
Empirical formula	C <sub>24</sub> H <sub>21</sub> Ag <sub>2</sub> Cl <sub>3</sub> F <sub>12</sub> N <sub>12</sub> Sb <sub>2</sub>	C <sub>24</sub> H <sub>21</sub> Ag <sub>2</sub> Cl <sub>3</sub> F <sub>12</sub> N <sub>12</sub> P 2	C <sub>6</sub> H <sub>5</sub> AgClF <sub>6</sub> N <sub>4</sub> Sb	C <sub>6</sub> H <sub>5</sub> AgClF <sub>6</sub> N <sub>4</sub> P
Formula weight	1271.12	1089.56	512.21	421.43
Temperature/K	100.00	100.01(10)	100.00(10)	100.00(10)
Crystal system	monoclinic	triclinic	monoclinic	monoclinic
Space group	P2 <sub>1</sub> /c	P-1	P2 <sub>1</sub> /c	P2 <sub>1</sub> /c
a/Å	16.2142(6)	8.0608(2)	12.0279(6)	11.9676(6)
b/Å	17.5601(5)	14.5789(3)	8.6719(4)	8.4366(4)
c/Å	13.5028(5)	16.1846(4)	12.8186(6)	12.5599(5)
α/°	90	72.495(2)	90	90
β/°	106.381(4)	82.655(2)	108.416(5)	108.484(5)
γ/°	90	74.413(2)	90	90
Volume/Å <sup>3</sup>	3688.5(2)	1744.90(8)	1268.57(11)	1202.70(10)
Z	4	2	4	4
ρ <sub>calc</sub> /g/cm <sup>3</sup>	2.289	2.074	2.682	2.327
μ/mm <sup>-1</sup>	2.813	1.549	3.947	2.098
F(000)	2416.0	1064.0	952.0	808.0
Crystal size/mm <sup>3</sup>	0.3 × 0.2 × 0.19	0.32 × 0.27 × 0.25	0.3 × 0.24 × 0.22	0.3 × 0.27 × 0.26
Radiation	Mo Kα (λ = 0.71073)	Mo Kα (λ = 0.71073)	Mo Kα (λ = 0.71073)	Mo Kα (λ = 0.71073)
2θ range for data collection/°	6.52 to 63.58	6.668 to 65.704	7.322 to 67.1	6.642 to 67.234
Index ranges	-23 ≤ h ≤ 23, -24 ≤ k ≤ 24, -18 ≤ l ≤ 16	-12 ≤ h ≤ 11, -21 ≤ k ≤ 22, -23 ≤ l ≤ 23	-18 ≤ h ≤ 16, -12 ≤ k ≤ 12, -19 ≤ l ≤ 18	-17 ≤ h ≤ 17, -11 ≤ k ≤ 12, -17 ≤ l ≤ 19
Reflections collected	43825	42398	16986	16396
Independent reflections	10487 [R <sub>int</sub> = 0.0590, R <sub>sigma</sub> = 0.0562]	11122 [R <sub>int</sub> = 0.0451, R <sub>sigma</sub> = 0.0446]	4338 [R <sub>int</sub> = 0.0487, R <sub>sigma</sub> = 0.0327]	4141 [R <sub>int</sub> = 0.0421, R <sub>sigma</sub> = 0.0362]
Data/restraints/parameters	10489/0/512	11122/12/527	4338/0/177	4141/6/202
Goodness-of-fit on F <sup>2</sup>	1.040	1.056	1.098	1.070
Final R indexes [I ≥ 2σ(I)]	R <sub>1</sub> = 0.0373, wR <sub>2</sub> = 0.0786	R <sub>1</sub> = 0.0389, wR <sub>2</sub> = 0.0762	R <sub>1</sub> = 0.0383, wR <sub>2</sub> = 0.0952	R <sub>1</sub> = 0.0338, wR <sub>2</sub> = 0.0790
Final R indexes [all data]	R <sub>1</sub> = 0.0612, wR <sub>2</sub> = 0.0858	R <sub>1</sub> = 0.0503, wR <sub>2</sub> = 0.0799	R <sub>1</sub> = 0.0422, wR <sub>2</sub> = 0.0969	R <sub>1</sub> = 0.0394, wR <sub>2</sub> = 0.0817
Largest diff. peak/hole / e Å <sup>-3</sup>	1.39/-1.15	1.82/-0.76	2.44/-1.70	2.58/-1.69

\*R<sub>1</sub> =  $\sum ||F_o| - |F_c|| / \sum |F_o|$  for  $F_o > 2\sigma(F_o)$ ; wR<sub>2</sub> =  $(\sum w(F_o^2 - F_c^2)^2 / \sum (wF_c^2)^2)^{1/2}$  all reflections  $w = 1 / [\sigma^2(F_o^2) + (0.1901P)^2 + 55.5750P]$  where  $P = (F^2 + 2F^2) / 3$

## 2.14 Vrf entries in CIFs with level B errors

### 2264862

Alert level B

PLAT910\_ALERT\_3\_B Missing # of FCF Reflection(s) Below Theta(Min). 14 Note 1  
0 0, 0 1 0, 1 1 0, 0 2 0, -1 -1 1, 0 -1 1, -1 0 1, 0 0 1, 1 0 1, 0 1 1, 1 1 1, 0 2 1, 0 0 2, 0 1 2

Author Response:

These low-angle reflections are probably missing due to the beam stop or were affected by unexpected deviations in their intensities for symmetry equivalent measurements and omitted during initial data reduction.

### 2264865

Alert level B

PLAT910\_ALERT\_3\_B Missing # of FCF Reflection(s) Below Theta(Min). 14 Note 1  
0 0, 2 0 0, 1 1 0, 2 1 0, 0 2 0, 1 2 0, -2 1 1, -1 1 1, 0 1 1, 1 1 1, -1 2 1, 0 2 1, -1 0 2, 0 0 2

Author Response:

These low-angle reflections are probably missing due to the beam stop or were affected by unexpected deviations in their intensities for symmetry equivalent measurements and omitted during initial data reduction.

## 2.15 Calculation of anion density in each crystal:

$$\text{Anion density (cm}^{-3}\text{)} = \frac{Z \times \text{no. of anions per asymmetric unit}}{\text{volume (in cm}^3\text{)}}$$

$$\begin{aligned}\text{Anion density of ACPSbF}_6 &= \frac{4 \times 2}{(3688.5 \times 10^{-8} \text{ cm})^3} \\ &= 2.169 \times 10^{21} \text{ cm}^{-3}\end{aligned}$$

$$\begin{aligned}\text{Anion density of ACPPF}_6 &= \frac{2 \times 2}{(1744.9 \times 10^{-8} \text{ cm})^3} \\ &= 2.28 \times 10^{21} \text{ cm}^{-3}\end{aligned}$$

$$\begin{aligned}\text{Anion density of MCPSbF}_6 &= \frac{4 \times 1}{(1268.57 \times 10^{-8} \text{ cm})^3} \\ &= 3.15 \times 10^{21} \text{ cm}^{-3}\end{aligned}$$

$$\begin{aligned}\text{Anion density of MCPPF}_6 &= \frac{4 \times 1}{(1202.7 \times 10^{-8} \text{ cm})^3} \\ &= 3.3 \times 10^{21} \text{ cm}^{-3}\end{aligned}$$

### 3 Device fabrication and optimization of $\text{MCPSbF}_6$

Two terminal lateral devices were fabricated on precleaned glass substrates. The substrates were cleaned by sequential ultrasonication in Triton X-100, DI water, Acetone and IPA for 15 minutes each and the substrates were treated with UV Ozone plasma. Thereafter Cr/Au electrodes were deposited by thermal vapor deposition method. . MOF solution was then drop casted and dried in atmosphere on these substrates to complete the fabrication process. The step-by-step procedure is provided in the following schematic **figure S24**

The step-by-step procedure is provided in the following diagram.

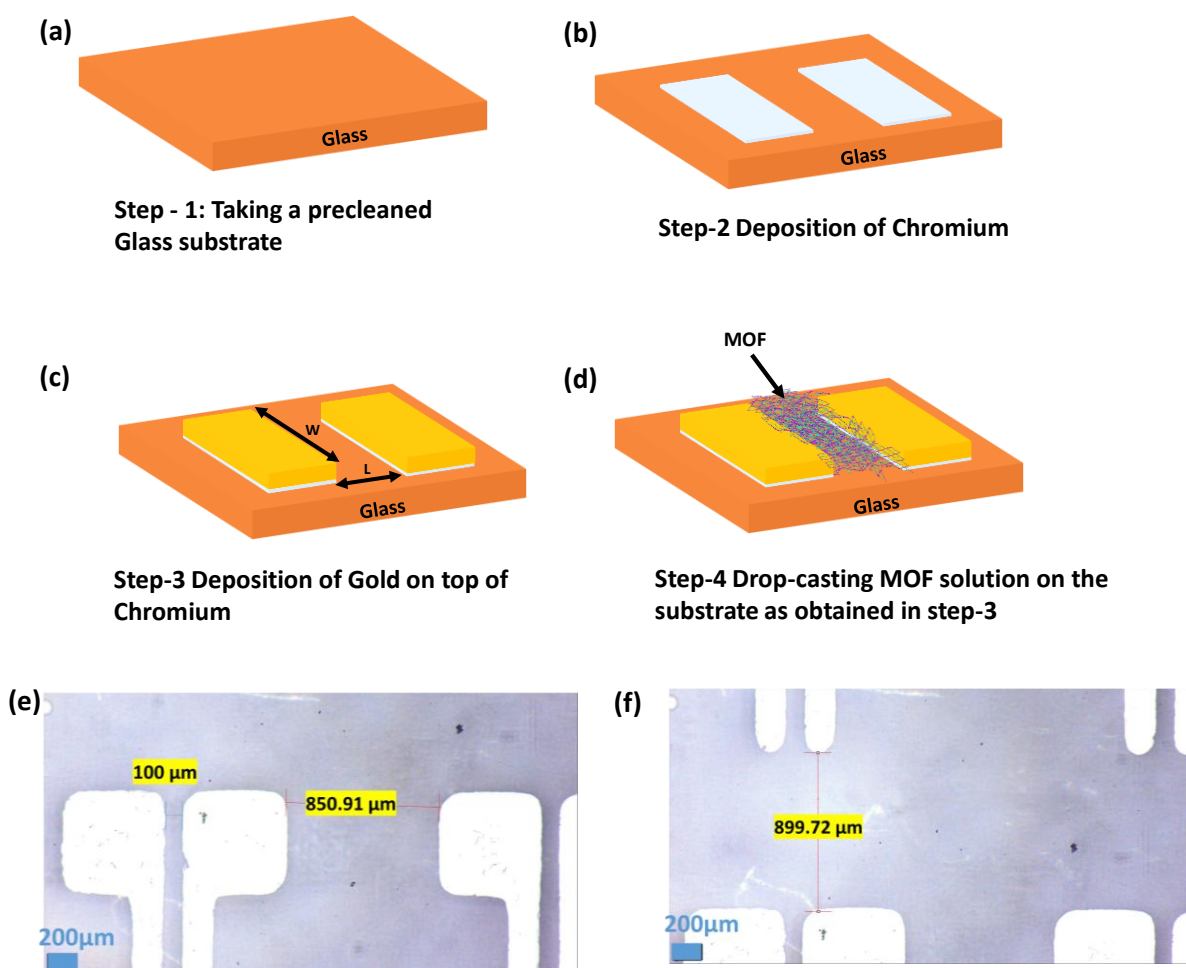


**Figure S24:** (a-d) Step-by-step process of the device fabrication. Optical microscopic image of device substrate with a channel length of  $100\ \mu\text{m}$ : (e) The horizontal distance between the two pairs of electrodes is  $850\ \mu\text{m}$ ; (f) The vertical distance between the two electrode pairs is  $900\ \mu\text{m}$ .

To optimize the two-terminal lateral devices,  $100\ \mu\text{l}$  of the individual molecules were drop cast on the pre-cleaned glass substrates with patterned electrodes. The films were fabricated using two strategies: one where it was dried at room temperature for 30 minutes and another where annealing was performed at  $80^\circ\text{C}$  for 15 minutes. IV

characteristics measured on these lateral two terminal devices demonstrate higher channel current ( $10^2$  times) for the devices fabricated by drying at room temperature (**Figure S25**). Hence, this method of film formation was followed for all the molecules. Considering the room temperature processibility of the device, we also fabricated flexible devices using the same method (an optical photo of such a device is shown in **Figure S25b**), which exhibits a similar level of performance as brittle devices.

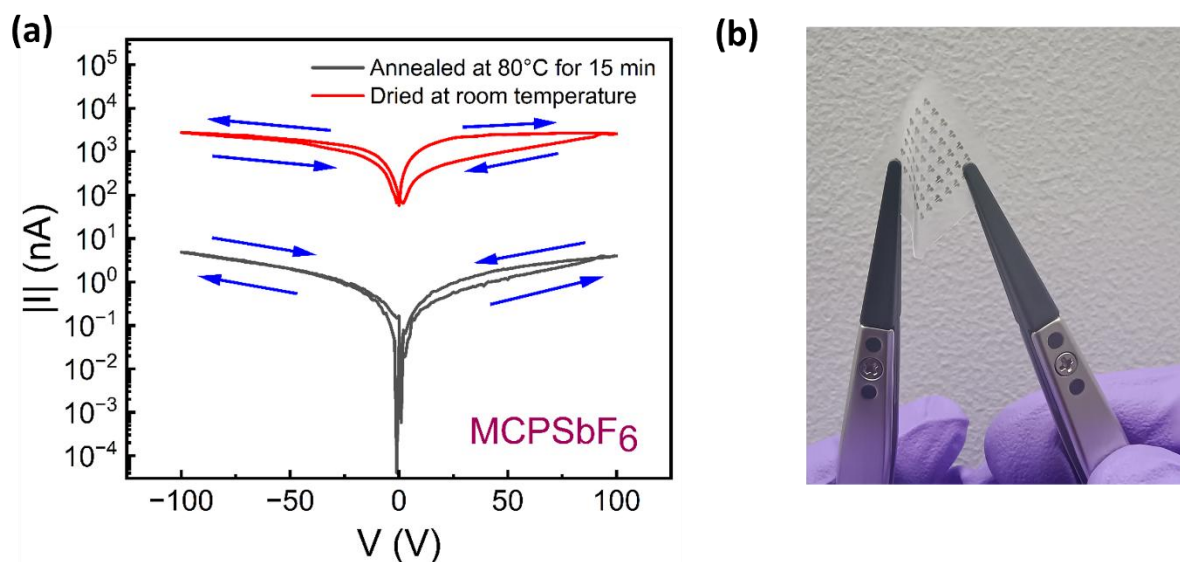


**Figure S25.** (a) IV characteristics from thin films of MCPSbF<sub>6</sub> prepared under different conditions as specified in the legend. (b) Optical photograph of a flexible device fabricated with MCPSbF<sub>6</sub>

## 4 Scan rate dependence measurement

To understand the reason behind the observed hysteretic I-V characteristics, we performed scan rate dependence measurement. The scan rate of an I-V sweep is estimated by dividing the voltage step size by the sum of integration time and delay time<sup>6</sup>. Scan rate-dependent I-V measurements were taken by setting different values of integration time and delay time in the B1500A semiconductor parameter analyzer (**Table S2**). The scan rate varied from 4 V.s<sup>-1</sup> to 500 V.s<sup>-1</sup> while keeping the voltage step size fixed at 2 V for these measurements. I-V characteristics measured at different scan rates exhibit a trend where the hysteresis increases as we lower the scan rate (**Figure 3b, Figure S26a-d**). Correspondingly, the I-V characteristics measured at a lower scan rate indicate lower channel current owing to significant screening of the gate potential. Note that the possibility of a current decrease due to bias stress in slower scans cannot be completely ignored in these measurements. Nevertheless, these results verify that ionic screening is the dominant contributor to the hysteresis in these materials.

**Table S2:** I-V scan rates determined from integration time and delay time.

Scan rate (V.s <sup>-1</sup> )	Integration time (ms)	Delay time (ms)
4	20	480
10	20	180
20	20	80
50	20	20
100	20	0
200	10	0
500	4	0
1000	2	0
5000	0.4	0
10000	0.2	0

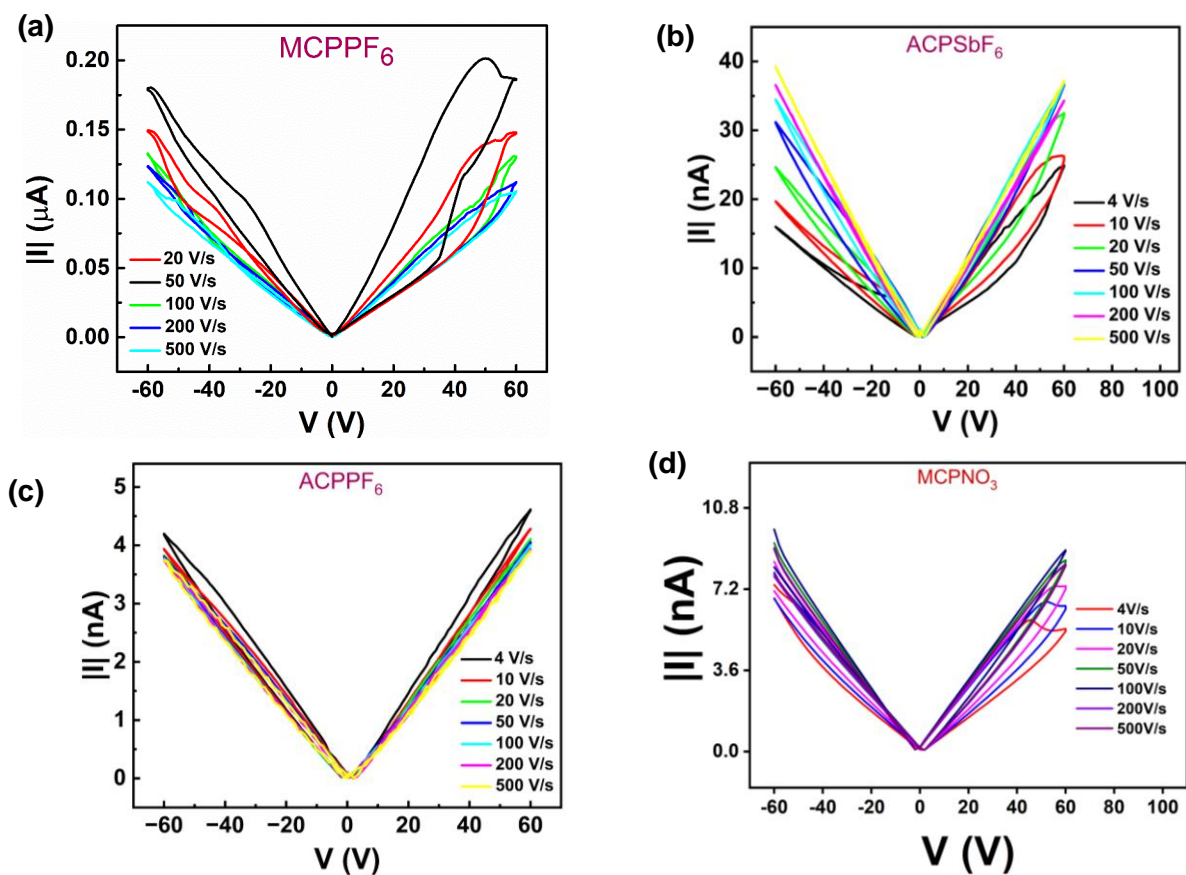


**Figure S26.** I-V characteristics of (a) MCPPF<sub>6</sub>, (b) ACPSbF<sub>6</sub>, (c) ACPFF<sub>6</sub>, and (d) MCPNO<sub>3</sub> were measured at different scan rates.

## 5 I-V Characteristics of the memristor device for varied channel lengths

Since our memory devices have channel length  $L = 100\mu\text{m}$  and channel width ( $W$ ) =  $1\text{mm}$ , hence we utilized an operating voltage in the range of  $40\text{V}$  to  $100\text{V}$ , which is apparently high. However, in terms of the effective electric field, these voltages correspond to only  $0.4\text{V}/\mu\text{m}$  to  $1\text{V}/\mu\text{m}$ , which is significantly less than most of the reported literature provided in **Table S4**. The usage of high voltages is directly related to the larger channel length used in our study. To confirm this, we prepared  $\text{MCPSbF}_6$  lateral devices with varied channel lengths ranging from  $20\mu\text{m}$  to  $100\mu\text{m}$ . I-V measurements were performed on these devices with different voltages while keeping the effective field the same, as shown in **Figure S27**. We observed that the current values remain around  $1\mu\text{A}$  for all the devices, indicating that channel length is just a scaling factor and the memristors can be operated at lower voltages, given that a device with a smaller channel length is utilized.

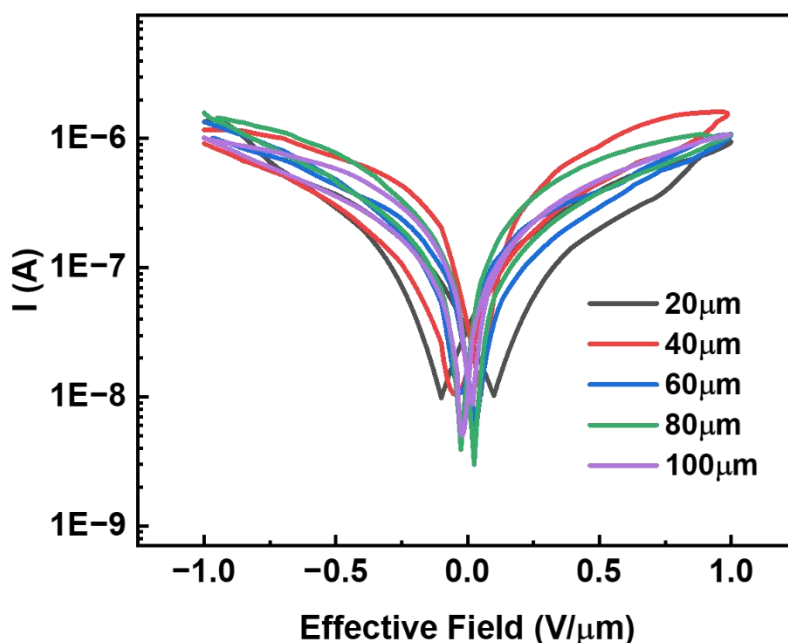


**Figure S27.** I-V characteristics were measured on lateral devices fabricated from  $\text{MCPSbF}_6$ -based devices with varied channel lengths ranging from  $20\mu\text{m}$  to  $100\mu\text{m}$ ; voltage values in sweeps were scaled according to the channel lengths to keep the effective electric field the same (maximum  $1\text{V}/\mu\text{m}$ ).

## 6 Vacuum dependence measurement

To further verify the ionic contribution to the I-V characteristics, we performed the I-V measurements on these lateral devices in a vacuum. The channel current decreases by around 4 orders of magnitude as the vacuum level is increased from 1 bar to 0.008 mbar, indicating that either compound is unstable under vacuum or vacuum probably removes the trapped solvents in the film, which can possibly help in the ionic migration in these devices (**Figure S28**), which further indicates that ions are the major contributor of conduction in these MOFs.

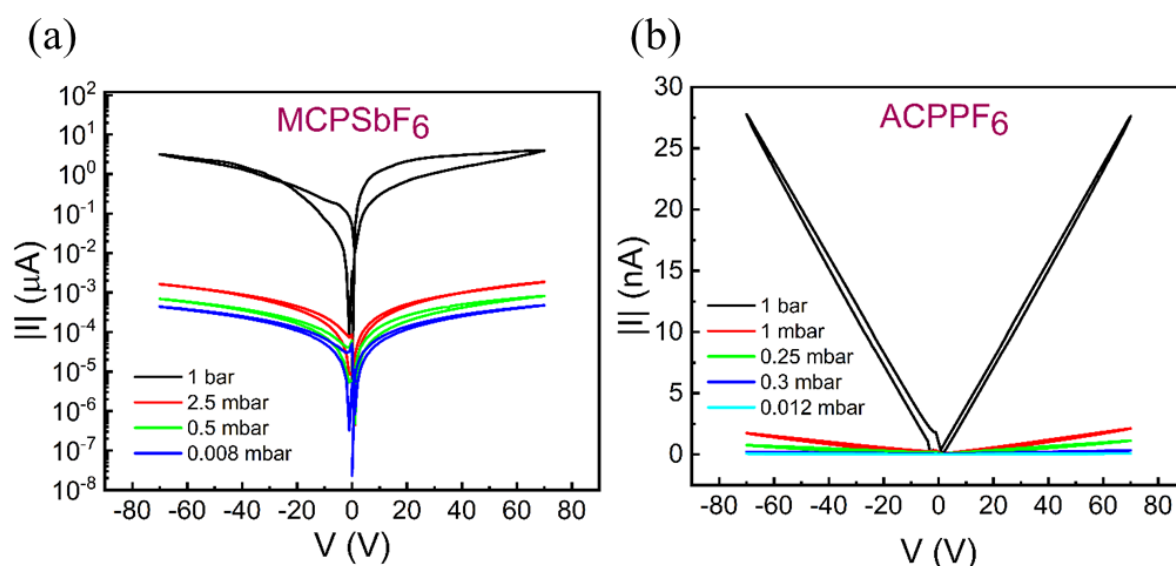


**Figure S28.** I-V characteristics of (a) MCPSbF<sub>6</sub> and (b) ACPPF<sub>6</sub> measured at different levels of pressure.

## 7 Voltage dependence measurement

Since the hysteretic characteristics in these devices are majorly attributed to ionic movement, increasing the voltage increases the effective field for ion migration. As the maximum voltage for the scan increases, the number of ions attracted to the electrodes increases, leading to increased ionic screening and, thereby, the hysteresis observed. To observe this behavior, we increased the voltage range from 10V to 100V in the step of 10V. **Figure 3c** and **Figure S29a-c** show that increasing the voltage range increases the ion screening effect, which results in larger hysteresis.

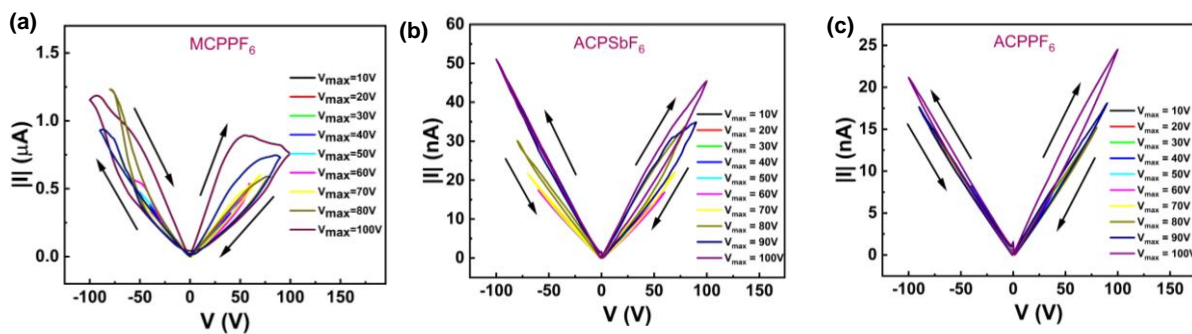


**Figure S29.** I-V characteristics of (a) MCPPF<sub>6</sub> (b) ACPSbF<sub>6</sub> (c) ACP PF<sub>6</sub> measured by increasing voltage range from  $\pm 10$  V to  $\pm 100$  V at a step size of 10 V on a lateral device  $L = 100 \mu\text{m}$ ,  $W = 1\text{mm}$ .

## 8 Ionic Conductivity measurement

The combined conductivity of electrons and ions was estimated by applying Ohm's law on I-V characteristics at a higher scan rate (10000 V/s) such that there is no hysteresis<sup>7</sup>. A constant current was applied to the device to measure the electronic conductivity. The electronic conductivity is calculated from the saturation regime in the time evolution of the resistance curve where there is no ionic movement<sup>7</sup>. The ionic conductivity is determined by subtracting the electronic conductivity from the total conductivity. Notably, for MCPSbF<sub>6</sub>, we are not able to obtain a hysteresis-free I-V sweep of 60V even at a 10000 V/s scan rate; hence, we have performed an I-V scan at a lower voltage of 10V at a 10000 V.s<sup>-1</sup> scan rate. **Figure S30a** indicates that the total conductivity is not affected by changing the voltage range. Due to the different magnitudes of ion movement in different molecules, the constant current for the electronic conductivity measurement was varied accordingly, and respective values are mentioned in the figure and figure captions. Note that because of higher ionic movement, a saturation region cannot be achieved at a lower constant current of 20pA (**Figure S30b**). Hence, for estimating the electronic conductivity, the constant current was increased to 2nA, and a similar strategy was implemented for all the molecules wherein it was difficult to observe the saturation regime.

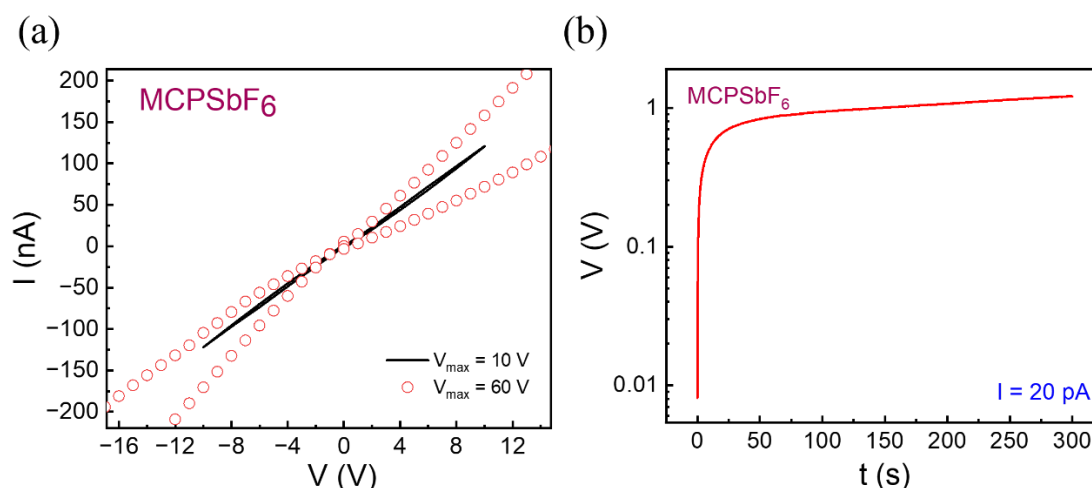


**Figure S30.** (a) Comparison of I-V characteristics with  $V_{\text{max}} = 10$  V & 60 V for MCPSbF<sub>6</sub> at 10000 V.s<sup>-1</sup> scan rate. (b) The voltage across the electrodes doesn't saturate in 300 s when a constant current of 20 pA is applied to MCPSbF<sub>6</sub>.

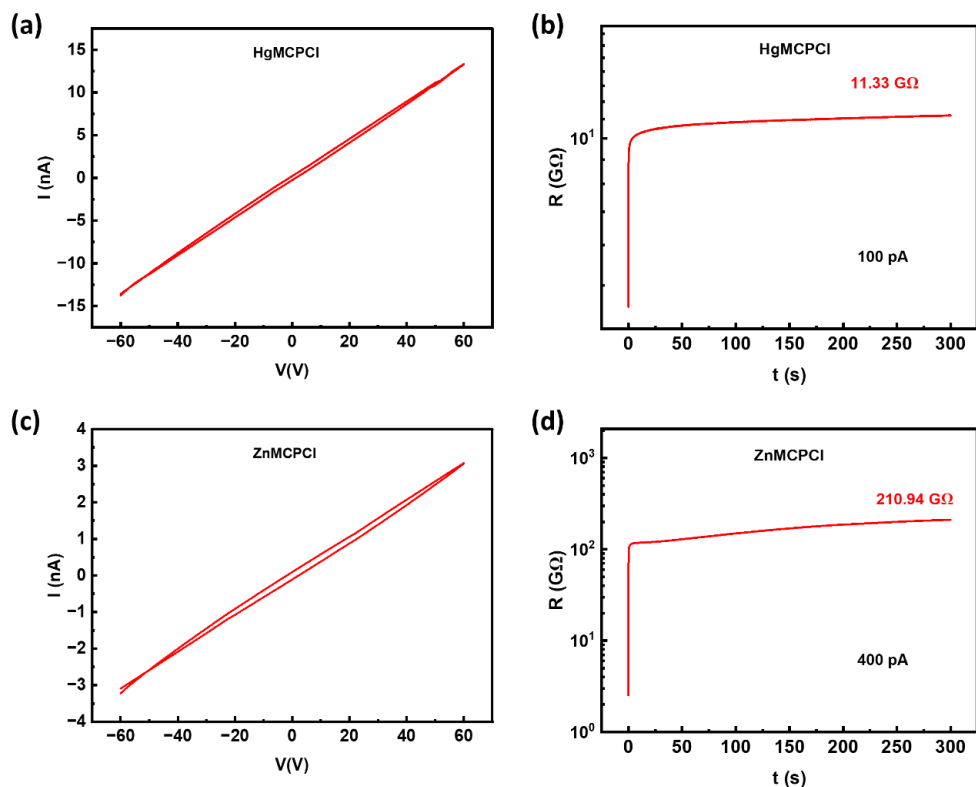


**Figure S31.** (a) and (c) I-V characteristics measure at a 10000V/s scan rate to estimate total conductivity for MOFs HgMCPCl and ZnMCPCl, respectively. (b) and (d) Galvanostatic measurement is used to estimate the electronic conductivity of the same MOFs. Corresponding constant current values are shown as inset of the figures along with the resistance value.

**Table S3: Electronic and ionic conductivity of different MOF complexes**

Molecule	$\sigma_e$ (S.m <sup>-1</sup> )	$\sigma_{ion}$ (S.m <sup>-1</sup> )
MCPSbF <sub>6</sub>	$3.3 \times 10^{-5}$	$4.8 \times 10^{-2}$
MCPPF <sub>6</sub>	$1.2 \times 10^{-4}$	$1.3 \times 10^{-2}$
ACPSbF <sub>6</sub>	$1.7 \times 10^{-4}$	$8.3 \times 10^{-4}$
ACPPF <sub>6</sub>	$1.8 \times 10^{-4}$	$6.6 \times 10^{-4}$
HgMCPCl	$3.5 \times 10^{-4}$	$5.2 \times 10^{-4}$
ZnMCPCl	$1.9 \times 10^{-5}$	$1.8 \times 10^{-4}$
MCPNO <sub>3</sub>	$4.2 \times 10^{-4}$	$9.8 \times 10^{-5}$

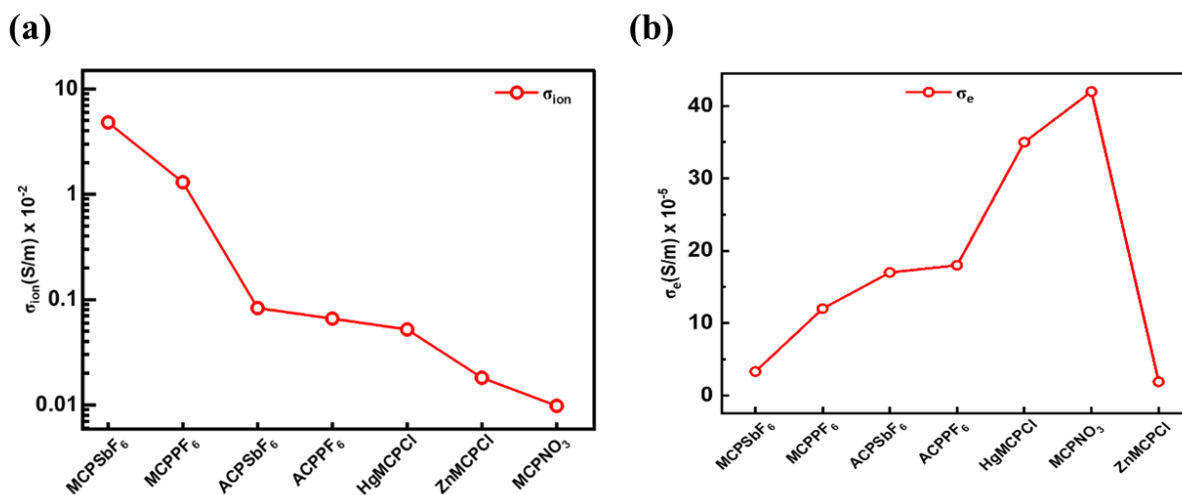


**Figure S32.** (a) Plot of (a) ionic conductivity ( $\sigma_{ion}$ ) (b) electronic conductivity ( $\sigma_e$ ) variation for different MOFs using a lateral device ( $L = 100 \mu\text{m}$ ,  $W = 1\text{mm}$ ) geometry consisting of Cr/Au electrode.

### Ionic Conductivity ( $\sigma_{ion}$ ) analysis for different categories of MOF (Figure S28a):

#### a) 2D MCP-MOFs with M-M Bonds and non-coordinating anions:

- **MCPSbF<sub>6</sub>:** Exhibits the highest ionic conductivity of  $4.8 \times 10^{-2} \text{ S/m}$  among these MOFs.
- **MCPPF<sub>6</sub>:** Exhibits the second-highest ionic conductivity of  $1.3 \times 10^{-2} \text{ S/m}$  among these MOFs.

The data reveals that 2-D MOFs with M-M bonds exhibit higher  $\sigma_{ion}$  values. This can be attributed to ion channels in rigid structures and the flexibility of Ag-Ag bond distance, which allows for the retention of the framework while anions are transported through the channels in multiple directions. Moreover, these two MOFs have the highest density of non-coordinating anions (Calculated in SI section 2.13).

#### b) 1D ACP-MOFs structures with M-M bond and non-coordinating anions:

- **ACPSbF<sub>6</sub>:** The ionic conductivity drops significantly by two orders of magnitude to  $8.3 \times 10^{-4} \text{ S/m}$ .
- **ACPPF<sub>6</sub>:** Similarly, it has an ionic conductivity of  $6.6 \times 10^{-4} \text{ S/m}$ .

With the change in the ligand from MCP to ACP, the dimensionality of the framework changes from 2-D to 1-D. Consequently, the number of  $\text{Ag}^+$  and the counter-anions decreases by  $\sim 30\%$ . Due to the limited availability of open channels for ion movement

in these lower dimensional structures and lower anion concentration, there is a sharp decrease in the ionic conductivity.

**c) 1D structure with M-M Bond interaction and coordinated anions:**

- **HgMCPCl:** has an ionic conductivity of  $5.2 \times 10^{-4}$  S/m.
- **MCPNO<sub>3</sub>:** Shows the lowest ionic conductivity of  $9.8 \times 10^{-5}$  S/m.

The ionic conductivity significantly drops due to the coordination of the metal cations (Hg and Ag) and the respective anions (Cl<sup>-</sup> and NO<sub>3</sub><sup>-</sup>). The reduced conductivity in MCPNO<sub>3</sub> is most likely due to the strong coordination of the nitrate anion with silver, compared to the chloride anion coordinated with the mercury metal.

**d) Discrete complexes without M-M bonds and coordinating ions:**

- **ZnMCPCl:** Exhibits very low ionic conductivity of  $1.8 \times 10^{-4}$  S/m.

This low conductivity can be attributed to the discrete MOFs as well as the presence of a coordination bond between Zn<sup>2+</sup> and anion (Cl<sup>-</sup>).

**Electrical Conductivity ( $\sigma_e$ ) Analysis (Figure S32b)**

In general,  $\sigma_e$  follows an inverse trend with respect to  $\sigma_{ion}$  for structures with M-M bonds where suitable channels for electron delocalization exist. This behavior can possibly be attributed to the effects of ionic screening. MCPNO<sub>3</sub> offers direct conduction pathways through Ag-Ag bonds (as illustrated in Figure S20) without any ligands interfering between these bonds. Consequently, it exhibits the highest electronic conductivity among all MOFs. A deviation in the trend is observed for ZnMCPCl, where the electronic conductivity is significant ( $1.9 \times 10^{-5}$  S/m). This is likely due to its discrete structure lacking M-M (Zn-Zn) interactions.

While the highest ionic conductivity of MCPSbF<sub>6</sub> is ~500 times more than the lowest ionic conductivity in MCPNO<sub>3</sub>, the ratio of the highest electronic conductivity to the lowest conductivity is only 12. This indicates that the electronic conductivity remains relatively consistent across all the MOFs studied. At the same time, ionic transport is significantly influenced by the type of anions and structure of the MOF. As mentioned earlier, both electrical and ionic conductivity are crucial for memory performance. However, ionic conductivity plays a more significant role in memory and neuromorphic computing than electronic conductivity.

## 9 Computational Methods

We employ density functional theory (DFT) implemented in the CP2K package to study the structural, electronic, and ion transport in metal-organic framework (MOF) structures. A single k-point is used as the k-mesh. All the simulations use Grimme-type (DFT-D3) dispersion corrections with the cut-off of 350 Ry, mixed Gaussian and plane-wave methodology employed in the QUICKSTEP formalism, PBEsol-GGA as exchange-correlation functional, and analytical dual-space pseudopotentials. The basis set used was a double-zeta valence polarized (DZVP) basis set optimized for molecular calculations (MOLOPT).

The crystal structures of MCP and ACP MOFs are constructed within a monoclinic framework based on experimental data. We used a 2\*2\*1 supercell (384 atoms; 16 formula units) for MCP and a 2\*1\*1 (656 atoms; 16 formula units) supercell for ACP MOF. It is necessary to consider such a supercell to model the molecular defect and to study the molecule ion transport within these MOF structures. The conjugate gradient method is used until the forces on each atom of these MOF structures become less than 0.01 eV/Å. The calculated lattice constants are obtained with  $a = 23.93 \text{ \AA}$ ,  $b = 16.87 \text{ \AA}$ , and  $c = 12.05 \text{ \AA}$  for MCP $\text{PF}_6$  MOF;  $a = 24.06 \text{ \AA}$ ,  $b = 17.34 \text{ \AA}$ , and  $c = 12.16 \text{ \AA}$  for MCP $\text{SbF}_6$  MOF, and  $a = 32.43 \text{ \AA}$ ,  $b = 17.56 \text{ \AA}$ , and  $c = 12.95 \text{ \AA}$  for ACP $\text{PF}_6$  MOF. These values are comparable to the experimental results obtained from XRD data, as shown in Table S1.

Also, the computational modeling of ion conduction in MOF using a nudged elastic band (NEB) method is well-developed and extensively studied in many studies. We employ the climbing-image nudged elastic band (CI-NEB) method to determine the minimum energy path (MEP) for diffusion. The convergence criterion of the total energy is  $1 \times 10^{-6}$  eV. The force convergence is set up as 0.015 eV/Å in the CI-NEB calculations. The linear interpolation between the endpoints is used to prepare initial guessed MEPs using 8 intermediate images. The activation energies for defect-induced molecule ion transport processes are calculated by evaluating the energy difference between the diffusing species in their ground-state configuration and at the saddle point during the migration.

## 10 Structural Details

In this study, we utilize 6-chloro-N7-methylpurine (MCP) (shown in **Figure 2b**) and 6-chloro-N7-allylpurine (ACP) (**Figure 1b**) as MOF structures, investigating the impact of molecular substitution on them. Our goal is to understand how substituting  $\text{XF}_6^-$  molecules (where X = P, Sb) influences their properties.

MCP: The MCP MOF structures are modeled based on experimental crystal structures. In this configuration, silver (Ag) acts as the metallic node, and 6-chloro-7-methylpurine serves as the organic linker. The porous framework is established through coordination bonds of Ag with specific nitrogen atoms (Ag-N<sub>z</sub> bonds, where z=1,3,7) (**Figure 2c**). The resulting bond lengths of Ag-N<sub>1</sub>, Ag-N<sub>3</sub>, and Ag-N<sub>7</sub> are 2.54 Å, 2.17 Å, and 2.2 Å,

respectively. The interatomic distance between two silver atoms (Ag-Ag) is determined to be 2.98 Å. To investigate the influence of molecular substitution and their interaction with the framework, we introduce PF<sub>6</sub> and SbF<sub>6</sub><sup>-</sup> molecules in each MCP MOF structure, resulting in two inequivalent models: MCPPF<sub>6</sub> and MCPSbF<sub>6</sub> (**Figure S33a,b**, respectively).

ACP: The ACP MOF structure also adopts a monoclinic arrangement, with silver (Ag) serving as the metallic node and 6-chloro-7-allylpyridine as the organic linker. The porous framework is established through Ag<sub>1</sub>-Ag<sub>2</sub> and Ag-N<sub>z</sub> (z= 1,3,9) bonds (shown in **Figure 1c**). Specifically, Ag<sub>1</sub> coordinates with N<sub>3</sub> atoms, while Ag<sub>2</sub> coordinates with N<sub>9</sub> atoms from three linker molecules. Additionally, a notable Ag<sub>2</sub>-N<sub>1</sub> coordination bond involves the N<sub>1</sub> atom from an adjacent layer's linker molecule. The resulting framework showcases distinct bond lengths: an Ag-Ag bond of 2.99 Å, and three Ag-N<sub>z</sub> bonds measuring 2.28 Å, 2.23 Å, and 2.24 Å. We introduce PF<sub>6</sub> and SbF<sub>6</sub><sup>-</sup> molecules in each of these ACP MOF structures, resulting in two inequivalent models: ACPF<sub>6</sub> and ACPSbF<sub>6</sub> (**Figure S33c,d**, respectively).

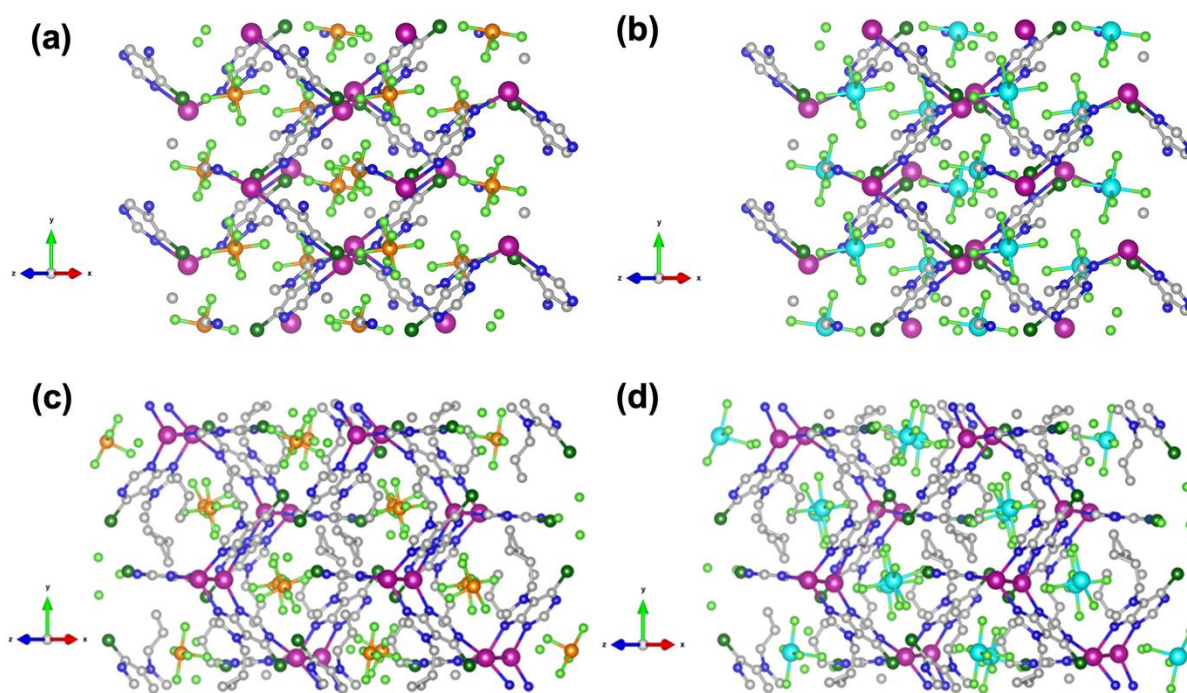


**Figure S33:** Structure of a) MCPPF<sub>6</sub>, b) MCPSbF<sub>6</sub>, c) ACPF<sub>6</sub>, and d) ACPSbF<sub>6</sub>. The color scheme for atoms aligns with **Figures 1** and **2**, with P represented in orange and Sb in cyan color.

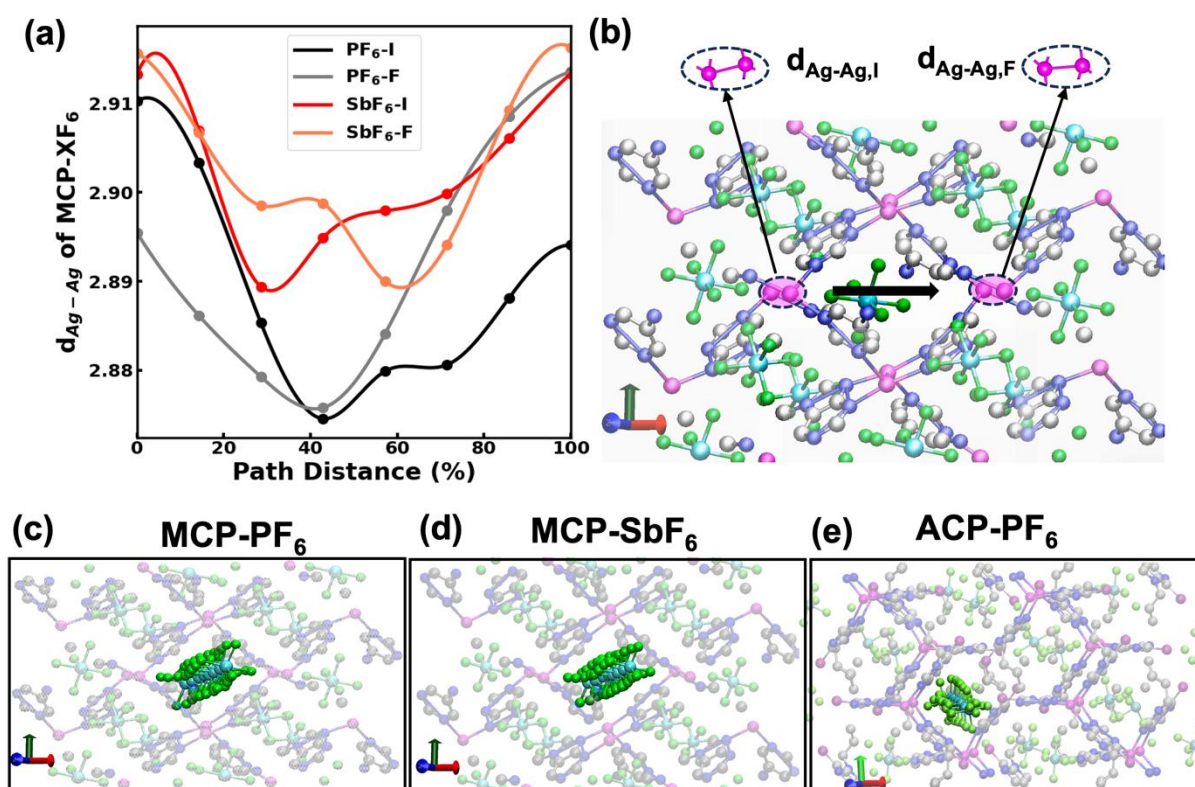


**Figure S34:** a) The distance between Ag-Ag ions, denoted as  $d_{(\text{Ag-Ag})}$ , in two instances: the distance between Ag ions in proximity to the initial position of migrating  $\text{XF}_6^-$  ion, represented as  $d_{(\text{Ag-Ag,I})}$  and denoted as  $\text{XF}_6\text{-I}$ , and the distance between Ag ions near the final position of migrating  $\text{XF}_6^-$  ion, represented as  $d_{(\text{Ag-Ag,F})}$  and denoted as  $\text{XF}_6\text{-F}$ . b) Schematics depicting the structural parameters  $d_{(\text{Ag-Ag,I})}$  and  $d_{(\text{Ag-Ag,F})}$ , with an arrow indicating the direction of migration of the  $\text{XF}_6^-$  ion. The migration pathways for c)  $\text{PF}_6^-$  migration through MCPPF<sub>6</sub> MOF, d)  $\text{SbF}_6^-$  migration through MCPSbF<sub>6</sub> MOF, and e)  $\text{PF}_6^-$  migration through ACPPF<sub>6</sub>-based MOFs.

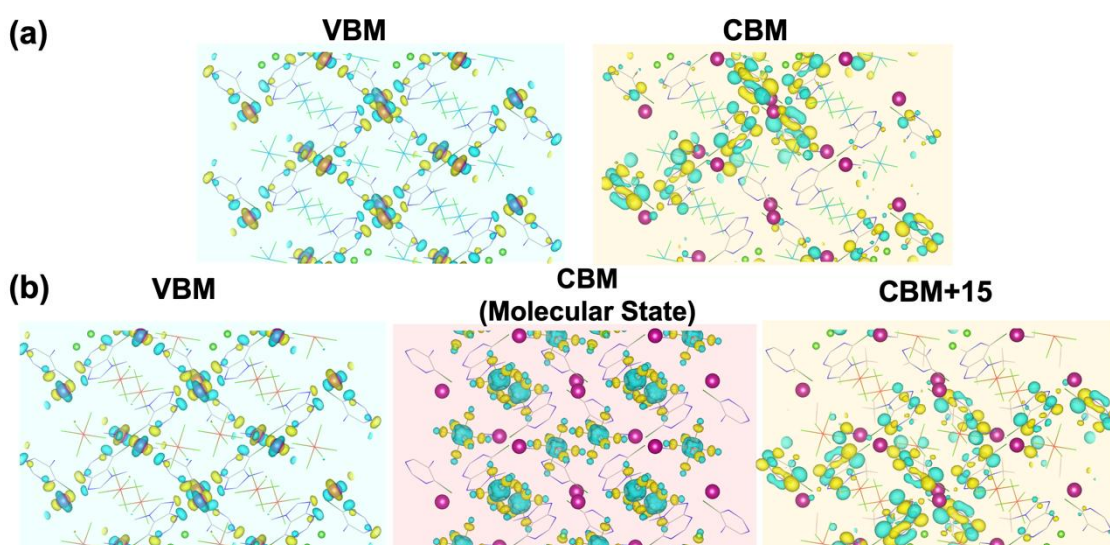


**Figure S35:** Charge density plot for a) VBM and CBM of MCPPF<sub>6</sub>, b) VBM, molecular midgap state, and CBM of MCPSbF<sub>6</sub>. All charge density plots are displayed with an isosurface value of 0.022/Å<sup>3</sup>.

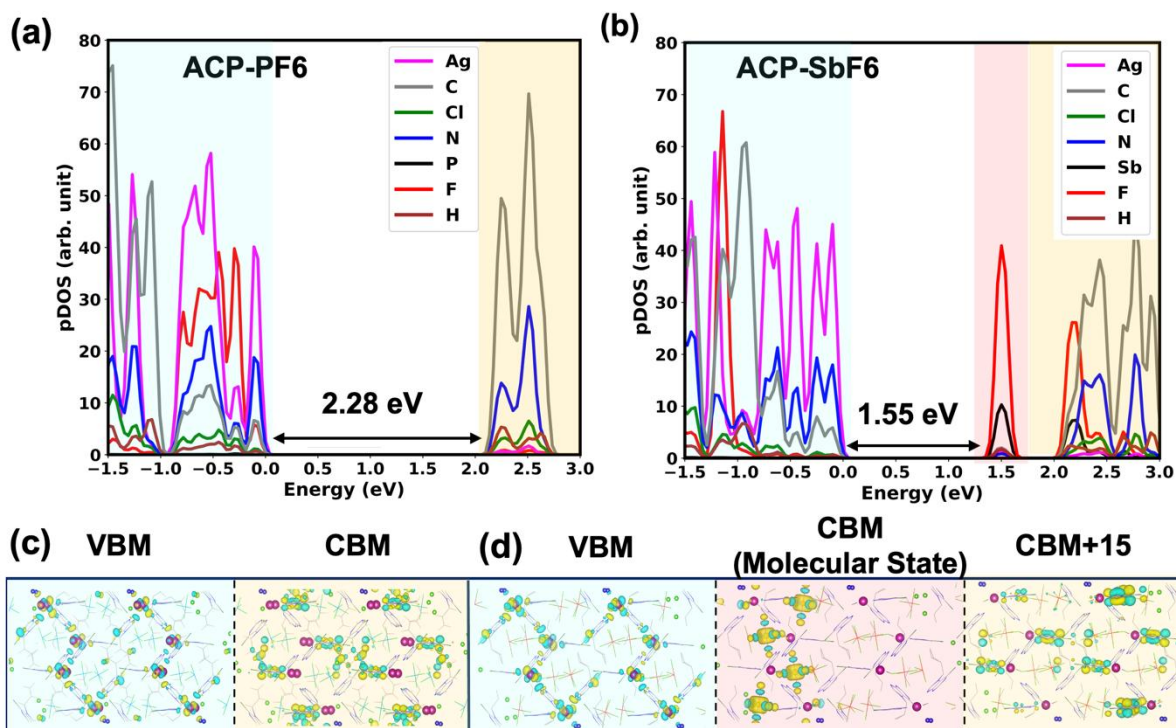


**Figure S36:** Partial density of state (PDOS) of a) ACP-PPF<sub>6</sub> and b) ACP-SbF<sub>6</sub>. Charge density plot for c) VBM and CBM of ACP-PPF<sub>6</sub>, d) VBM, molecular midgap state, and CBM of ACP-SbF<sub>6</sub>. All charge density plots are displayed with an isosurface value of 0.022/Å<sup>3</sup>.

## 11 Stability of the memory devices under Biasing

Both positive and negative biasing of the memory devices is required quite frequently for memory and neuromorphic operation. Such a wide variation of voltage may affect the structural integrity of the material and/or device. Therefore, prior to proceeding with such tests, XRD and SEM measurements were taken for the devices coated with MCPSbF<sub>6</sub> after performing multiple cycles of high-voltage sweeps. The devices were subjected to voltage biases of  $\pm 100$  V for up to 20 cycles, and then the XRD and SEM were performed to check for any structural disintegration. XRD pattern obtained on the devices in the range of  $2\theta = 0^\circ$  to  $50^\circ$  did not exhibit any change in the pattern (**Figure S37**). Note that the peak at  $38.2^\circ$  corresponds to the Au electrode on the device.

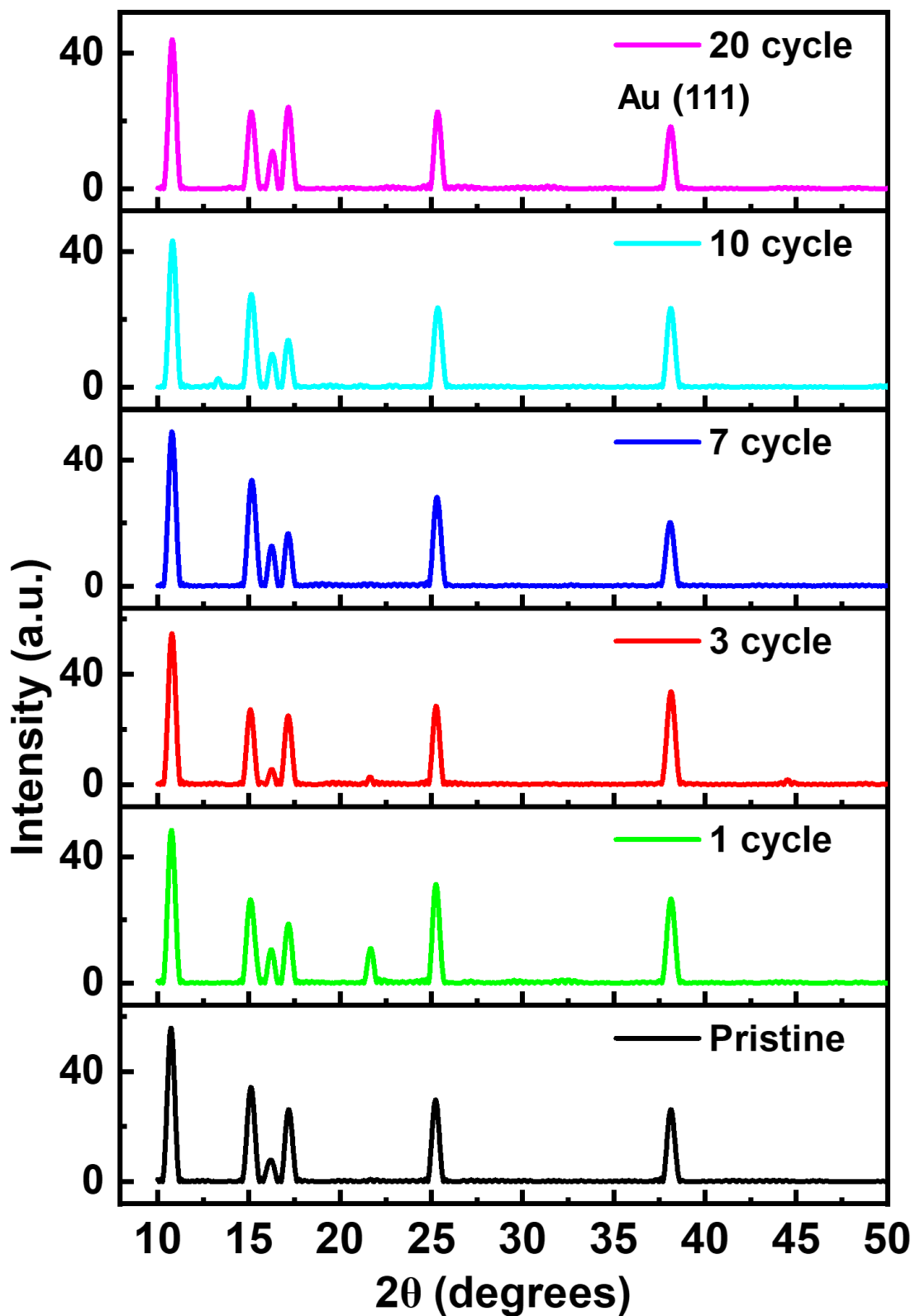


**Figure S37.** Variation in the diffraction pattern of thin film devices fabricated from  $\text{MCPSbF}_6$  upon multiple cycles of biasing at  $\pm 100$  V, which corresponds to an  $E_{\text{eff}} \sim 1\text{V}/\mu\text{m}$ .

Similarly, SEM measurements were performed on the devices for the EHT values ranging from 4-5 keV (**Figure S38**). Both the measurements confirm that bias stress does not significantly affect the device's structural integrity.

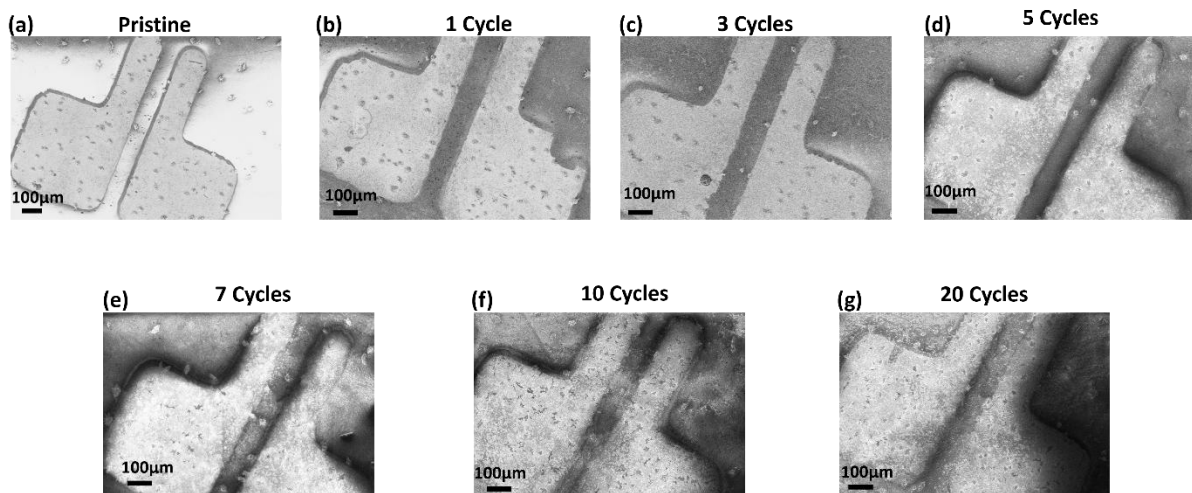


**Figure S38.** SEM image of different devices fabricated from  $\text{MCPSbF}_6$ , which are poled at  $\pm 100$  V (corresponding to an  $E_{\text{eff}} = 1 \text{ V}/\mu\text{m}$ ) for different number of cycles. The typical channel length is  $100 \mu\text{m}$  and  $W = 1 \text{ mm}$ . Mild discoloration was observed because of the charging of the samples while performing multiple SEM measurements on the same channel.

## 12 Endurance of the memory device.

The endurance of the memory device was tested in the volatile regime of operation by continuously switching it to LRS and HRS and monitoring the channel current at each state. The LRS state was achieved by programming the device with  $+0.1 \text{ V}/\mu\text{m}$  for 10s, and HRS was achieved by programming the device with  $-0.2 \text{ V}/\mu\text{m}$  for 10s. It was observed that LRS and HRS states can be distinctly identified up to 175 cycles of operations (**Figure S39**). Further optimization of the chemical design and device engineering can result in a higher level of endurance with such materials. We note that the devices exhibit relatively lower stability with a decrease in the ON/OFF ratio. This behavior can possibly be attributed to ionic defect induced screening of the applied potential and/or possible electrochemical degradation of the metal-MOF interface.

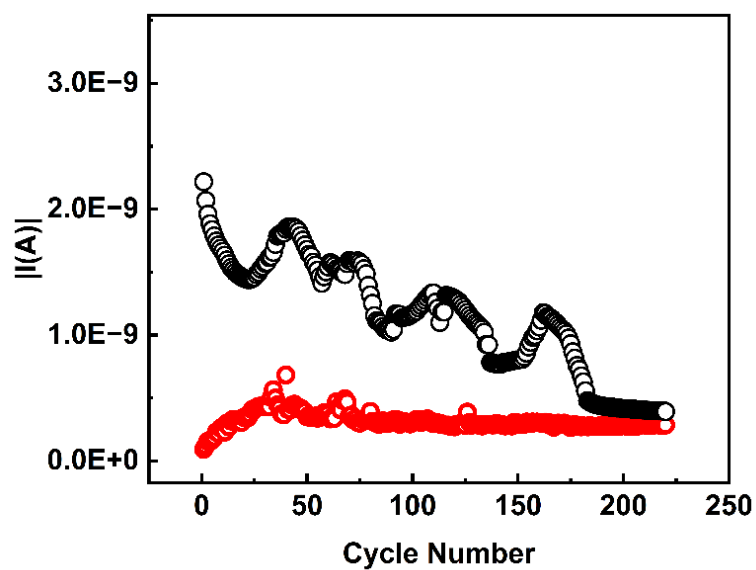


**Figure S39.** Endurance measurements were performed on two terminal devices depicting the absolute value of channel current. The LRS state is realized by programming at  $0.1\text{V}/\mu\text{m}$  for 10 seconds, and the HRS state is realized by poling at  $-0.2\text{V}/\mu\text{m}$  for 10 seconds.

# 13 Heterosynaptic Plasticity of MCPSbF<sub>6</sub> neuromorphic devices

## 13.1 Heterosynaptic Plasticity Measurements:

To observe the heterosynaptic plasticity of MCPSbF<sub>6</sub>, the current change across two inner electrodes (1-2,1-3,1-4,2-3,2-4,3-4) was observed after applying a field of 1V/μm and -1V/μm for 5 s across the outer electrodes (5-6) in six-terminal devices (a schematic of a 6-terminal device and electrode numbers are inset in **Figure 6d**). From the I-V curves (**Figure 6d, S40**) of six-terminal MCPSbF<sub>6</sub> neuromorphic devices, it was observed that MCPSbF<sub>6</sub> neuromorphic devices exhibit heterosynaptic plasticity and mimic multiple synaptic connections in neurons, which is evident from the fact that conductance between two inner electrodes (2-3) can be modulated by applying 1V/μm or -1V/μm pulse of 5s duration between its outer electrode (5-6) which are physically disconnected from the inner ones.

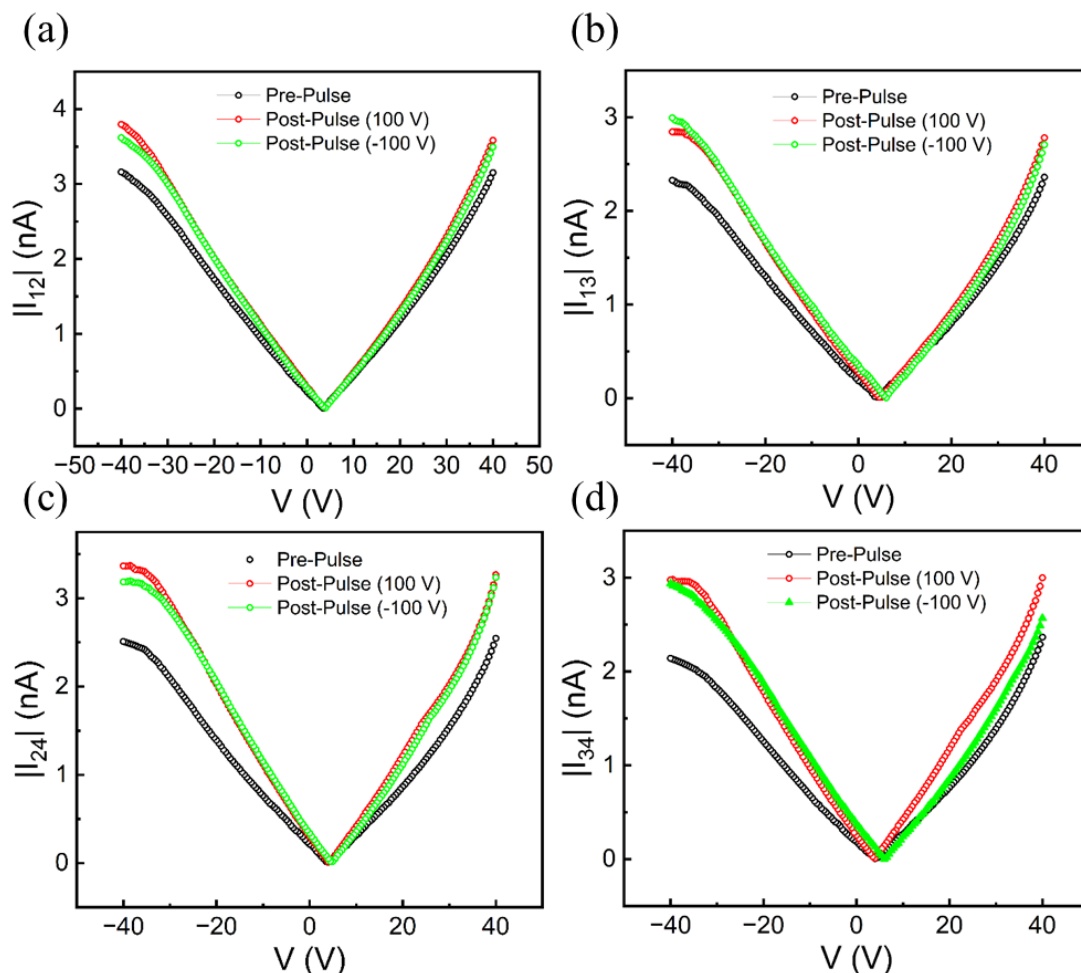


**Figure S40.** Heterosynaptic plasticity property represented by (a)  $|I_{12}|$  vs  $V_{12}$  (b)  $|I_{13}|$  vs  $V_{13}$  (c)  $|I_{24}|$  vs  $V_{24}$  (d)  $|I_{34}|$  vs  $V_{34}$  before and after applying 100V & -100V pulses for 5s between terminal 5 and 6. Schematic of the 6 terminal device structure is provided in the inset Figure 6d.

### 13.2 Estimation of energy consumption in heterosynaptic plasticity:

To calculate the energy consumption, we have considered highest bias value and corresponding current in the I-V sweep; multiplication of current and voltage gives power which was then multiplied with the time corresponding to scan rate to get energy consumption for each data obtained in synaptic current reading.

With respect to the Figure 6d, where we have estimated energy consumption to be in the range of 16-23 nJ; I-V sweep was taken in the range of -40 to +40V and the time for which a state is measured is 160 ms, which means energy was dissipated for this time-duration for any voltage value before moving to next voltage value in the sweep. The energy consumption was estimated by following method:

For Pre-Pulse:

$$V = 40 \text{ V},$$

$$I = 2.4954 \text{ nA}$$

$$P = 40 \times 2.4954 = 99.816 \text{ nW}$$

$$\begin{aligned} \text{Energy Consumption} &= 99.816 \text{ nW} \times 160 \text{ ms} \\ &= 15.97 \text{ nJ} \approx 16 \text{ nJ} \end{aligned}$$

For post-pulse (1 V/ $\mu\text{m}$ ):

$$V = 40\text{V}$$

$$I = 3.56677 \text{ nA}$$

$$P = 40 \times 3.56677 = 142.6708 \text{ nW}$$

$$\begin{aligned} \text{Energy Consumption} &= 142.6708 \text{ nW} \times 160 \text{ ms} \\ &= 22.83 \text{ nJ} \approx 23 \text{ nJ} \end{aligned}$$

For post-pulse (-1V/ $\mu\text{m}$ ):

$$V = 40\text{V}$$

$$I = 3.2149 \text{ nA}$$

$$P = 40 \times 3.2149 = 128.596 \text{ nW}$$

$$\begin{aligned} \text{Energy Consumption} &= 128.596 \text{ nW} \times 160 \text{ ms} \\ &= 20.58 \text{ nJ} \approx 21 \text{ nJ} \end{aligned}$$

Since the above-calculated values are for extreme points where both current and voltage are highest, the energy consumption for all other state's points should be in the range of 16-23 nJ.

# 14 Summary of memory and neuromorphic parameters for different devices

**Table S4:** Summary of memory and neuromorphic parameters from the literature.

Sl. No.	Active Material	Device Architecture	ILRS/IHRS	Programming Electric field(V/ $\mu$ m)	Endurance	Energy per spike	PPF % <sup>§</sup>	STDP ratio <sup>#</sup>	Ref
1.	<b>Ag-MOF</b>	<b>L</b>	<b>10<sup>7</sup></b>	<b>0.4</b>	<b>175</b>	<b>1 nJ</b>	<b>60</b>	<b>109.81<sup>*</sup></b>	<b>This work</b>
2.	HOF-FJU-52	V	10 <sup>9</sup>	-	10 <sup>6</sup>	347 zJ	-	-	8
3.	MoS <sub>2</sub> /hBN/F LG	V	10 <sup>7</sup>	5000	10 <sup>6</sup>	-	-	-	9
4.	COF-Auz	V	50	12.187	300	-	-	-	10
5.	Ta <sub>2</sub> O <sub>5</sub> /AlN/G	V	>10 <sup>2</sup>	200	5×10 <sup>4</sup>	37 fJ	27.5	5.45(+), 3.61(-)	11
6.	MP1	V	10 <sup>3</sup>	107.3	-	-	~3.7	-	12
7.	MHA-SAM-SURMOF-HKUST-1	V	~10 <sup>7</sup>	35	-	-	-	-	13
8.	MoS <sub>2</sub>	V	>10 <sup>2</sup>	26.67, -20	>500	600 fJ	80	3(+), 4.76 (-)	14
9.	TiN/AlN/G/Pd	V	>10 <sup>2</sup>	34, -68	-	-	160	8 (-), 9.56 (+)	15
10.	FJU-23-H2O	V	2 × 10 <sup>5</sup>	-	100	-	-	-	16
11.	COFBTA+PD A/	V	10 <sup>5</sup>	-46.48, 21.126	200	-	-	-	17
12.	AuNPs@ {[Cd (tib)2]·(ClO4) 2·(DMF)4}n	V	10 <sup>3</sup>	1.4	200	-	-	-	18
13.	AuNPs@ {[Cd (tib)(Tdc)]·(DMA)3}n	V	10 <sup>4</sup>	1.67	200	-	-	-	18
14.	AgNPs@ {[Cd (tib)2]·(ClO4) 2·(DMF)4}n	V	10 <sup>2</sup>	3.2	200	-	-	-	18
15.	AgNPs@ {[Cd (tib)(Tdc)]·(DMA)3}n	V	10 <sup>3</sup>	2.53	200	-	-	-	18
16.	Zn-TCPP@PVPy	V	~10 <sup>5</sup>	14.3	10 <sup>3</sup>	-	-	-	19
17.	Ti <sub>3</sub> C <sub>2</sub> T <sub>x</sub>	V	10 <sup>2</sup>	33.33, -26.67	10 <sup>6</sup>	-	+80/-60	13.19(+), 25.27(-)	20
18.	N-GOQD	V	10 <sup>7</sup>	2.37, 1.54	1.2×10 <sup>4</sup>	-	-	11.96(+), 3.54(-)	21
19.	ZHO/GO-QD	V	-	300	10 <sup>3</sup>	141 fJ	16	15.27(+), 17.49(-)	22
20.	MIL-53	V	~10 <sup>2</sup>	20	200	-	-	-	23
21.	MoS <sub>2</sub>	V	~50	2770, -1230.8	-	0.1 nJ	130	-	24
22.	AlOx	V	10 <sup>6</sup>	15.33	10 <sup>3</sup>	0.01-1 fJ	-	93.05(+), 25.02(-)	25
23.	[Ru(L)3](PF <sub>6</sub> ) <sub>2</sub>	V	10 <sup>4</sup>	8.125-8.75	10 <sup>12</sup>	-	-	-	26
24.	ZIF-8 in alcohol vapor	V	~10 <sup>7</sup>	20-40	25	-	-	-	27
25.	HKUST-1	V	18	6	106	-	-	-	28
26.	RS-MOF-1	V	30	-	-	-	-	-	29
27.	MoS <sub>2</sub> @ZIF-8	V	7 × 10 <sup>4</sup>	41.25	-	-	-	-	30
28.	Rb-CD-MOF	V	150	-	20	-	-	-	31
29.	MoS <sub>2</sub> /hBN/graphene	Transistor (MoS <sub>2</sub> )	10 <sup>4</sup>	1500	-	-	-	-	32
30.	Li <sub>x</sub> MoS <sub>2</sub>	L	~10	1.2	10 <sup>3</sup>	-	-	-	33

# Estimation of STDP Ratio: It is the ratio of synaptic weights at initial and final time intervals between the pre and post-synaptic pulses.  $STDP\ Ratio = \frac{\Delta w\ at\ \Delta t_{initial}}{\Delta w\ at\ \Delta t_{final}}$ ; where  $\Delta w$  is synaptic weight, and  $\Delta t$  is the time interval. A higher STDP ratio indicates enhanced learning capability and improved memory formation.

⌘ PPF Index: It is defined as the highest synaptic weight (in%), which is achieved at the lowest time interval between pre- and post-synaptic value.

### **A comparative advantage of our material and devices over the reported literature:**

- a) Our synthesis process offers a compelling advantage in terms of simplicity and efficiency. MCPSbF<sub>6</sub> can be readily prepared via room-temperature solution processability within just 30 minutes. The device is fabricated by drop-casting a methanolic solution of MCPSbF<sub>6</sub> on pre-patterned glass/Cr/Au substrates, which does not require any post-processing and can be easily scaled up for commercial and practical application.
- b) MCPSbF<sub>6</sub> and the rest of our MOFs are utilized as thin films. Thin films offer significant advantages over single crystals, such as (a) flexibility, (b) scalability, (c) ease of fabrication, and (d) solution processability.
- c) The underlying mechanism diverges significantly from previous reports; MCPSbF<sub>6</sub> relies on ion screening of anions (SbF<sub>6</sub><sup>-</sup>) modifying the electrical conductivity, while earlier memory devices rely on mechanisms such as electroforming, H-bond switching, ferroelectric transitions, etc, for the demonstration of memory devices.
- d) MCPSbF<sub>6</sub> poses high crystallinity, minimizes defect sites, and has a fixed ratio of ligand: metal: anions, leading to more consistent and predictable performance.
- e) MCPSbF<sub>6</sub> shows memory (both volatile and non-volatile) and neuromorphic computing (two-terminal and multi-terminal memory).

A comparison of the device parameters brings out the following aspects of MCPSbF<sub>6</sub>:

- a) It is one of the only memory devices based on lateral architecture, which allows easy scaling and seamless integration.
- b) Ultra-low programming electric field of  $\sim 0.4\ V/\mu m$ .
- c)  $\frac{I_{LRS}}{I_{HRS}} \sim 10^7$
- d) LRS-HRS retention time of more than  $10^4 s$ .
- e) Endurance retention of up to 175 cycles.
- f) Energy per spike of neuromorphic operation  $\sim 1\ nJ$ .
- g) PPF %  $\sim 60$
- h) STDP ratio of  $\sim 109$
- i) Symmetric Anti-Hebbian Learning.

## 15 Hydrogen bond tables.

**Table S5.** Hydrogen bonds for ACPSbF<sub>6</sub>

D-H...A	d(D-H)	d(H...A)	d(D...A)	<(DHA)
C(2)-H(2)...F(9)#3	0.93	2.42	3.335(5)	168.8
C(2A)-H(2A)...F(8)#3	0.93	2.53	3.296(5)	140.3
C(2B)-H(2B)...F(7)#3	0.93	2.63	3.261(4)	125.4
C(2B)-H(2B)...F(11)#3	0.93	2.57	3.485(5)	168.1
C(8)-H(8)...F(5)#4	0.93	2.65	3.465(5)	146.8
C(8)-H(8)...F(13 <sup>a</sup> )#4	0.93	2.29	3.05(3)	138.5
C(8A)-H(8A)...F(10)#5	0.93	2.37	3.179(5)	145.2
C(8B)-H(8B)...F(3 <sup>a</sup> )#1	0.93	2.48	3.355(5)	156.5
C(10)-H(10A)...Cl(1)	0.97	2.77	3.369(4)	120.9
C(10)-H(10B)...F(2)#4	0.97	2.40	3.259(5)	146.6
C(10)-H(10B)...F(13 <sup>a</sup> )#4	0.97	2.61	3.21(3)	120.2
C(10A)-H(10D)...F(10)#5	0.97	2.56	3.351(5)	138.6
C(10A)-H(10D)...F(12)#5	0.97	2.62	3.286(4)	125.6
C(10B)-H(10E)...F(4)#1	0.93(5)	2.49(5)	3.178(5)	131(3)
C(10B)-H(10F)...Cl(1B)	1.06(5)	2.78(5)	3.358(5)	115(4)
C(11)-H(11)...F(1 <sup>a</sup> )#4	0.93	2.60	3.214(5)	123.9
C(11)-H(11)...Cl(1)#6	0.93	2.87	3.514(4)	127.7
C(11B <sup>a</sup> )- H(11B <sup>a</sup> )...F(4)#7	0.93	2.52	3.221(7)	132.5
C(1 <sup>a</sup> )-H(1 <sup>a</sup> )...F(6)#1	0.93	2.60	3.373(16)	140.5

Symmetry transformations used to generate equivalent atoms:

#1 x, -y+1/2, z+1/2 #2 x, -y+1/2, z-1/2 #3 -x+1, -y+1, -z+1

#4 -x+2, -y+1, -z+2 #5 -x+1, -y+1, -z+2 #6 x, -y+3/2, z+1/2

#7 -x+2, y-1/2, -z+3/2

**Table S6.** Hydrogen bond table for ACPPF<sub>6</sub>

D-H...A	d(D-H)	d(H...A)	d(D...A)	<(DHA)
C(2)-H(2)...F(7)#4	0.93	2.50	3.186(4)	130.6
C(2)-H(2)...F(9)#4	0.93	2.59	3.516(4)	176.0
C(2A)-H(2A)...F(9)#5	0.93	2.62	3.427(4)	145.6
C(2B)-H(2B)...F(9)#5	0.93	2.43	3.321(4)	159.9
C(8A)-H(8A)...F(11)#1	0.93	2.59	3.322(4)	135.5
C(8B)-H(8B)...Cl(1B)#1	0.93	2.70	3.504(3)	144.8
C(10)-H(10A)...Cl(1)	0.97	2.87	3.344(4)	111.0
C(10)-H(10B)...F(2)#1	0.97	2.37	3.321(5)	166.5
C(10A)-H(10F <sup>a</sup> )...F(10)#6	1.03(13)	2.26(13)	3.285(4)	178(10)
C(10A)-H(10D <sup>a</sup> )...Cl(1A)	0.97	2.71	3.368(4)	125.7
C(10A)-H(10D <sup>a</sup> )...Cl(1B)#3	0.97	2.98	3.885(4)	156.2
C(10B)-H(10G)...Cl(1A)#3	0.97	2.94	3.714(4)	137.9
C(10B)-H(10H)...Cl(1B)	0.97	2.82	3.355(3)	115.5
C(11)-H(11)...Cl(1)	0.93	2.93	3.468(6)	118.0

C(11A <sup>a</sup> )-H(11A <sup>a</sup> )...Cl(1A)	0.93	2.75	3.356(11)	123.6
--	------	------	-----------	-------

Symmetry transformations used to generate equivalent atoms:

#1  $x-1, y, z$  #2  $-x, -y+2, -z+1$  #3  $-x+2, -y+1, -z+1$

#4  $x+1, y, z$  #5  $-x+1, -y+2, -z+1$  #6  $-x+1, -y+1, -z+1$

**Table S7.** Hydrogen bond table for MCPSbF<sub>6</sub>

D-H...A	d(D-H)	d(H...A)	d(D...A)	<(DHA)
C(10)-H(10A)...F(2)#4	0.98	2.53	3.325(6)	138.0
C(10)-H(10B)...F(2)#5	0.98	2.59	3.482(6)	150.8
C(10)-H(10C)...F(1)#6	0.98	2.43	3.168(6)	131.5
C(2)-H(2)...F(6)#1	0.95	2.45	3.342(6)	155.7
C(8)-H(8)...F(2)#5	0.95	2.44	3.283(5)	147.9
C(8)-H(8)...F(5)	0.95	2.56	3.338(6)	139.8
C(8)-H(8)...Cl(1)#2	0.95	2.82	3.339(4)	115.7

Symmetry transformations used to generate equivalent atoms:

#1  $-x, -y+1, -z+1$  #2  $x, -y+3/2, z+1/2$  #3  $x, -y+3/2, z-1/2$

#4  $x, -y+1/2, z-1/2$  #5  $-x+1, y+1/2, -z+3/2$  #6  $x, y+1, z$

**Table S8.** Hydrogen bond table for MCPFF<sub>6</sub>

D-H...A	d(D-H)	d(H...A)	d(D...A)	<(DHA)
C(2)-H(2)...F(4)#1	0.93	2.61	3.498(4)	159.3
C(8)-H(8)...Cl(1)#2	0.93	2.80	3.310(3)	116.0
C(8)-H(8)...F(1)#4	0.93	2.59	3.421(4)	148.8
C(10)-H(10A)...F(1)#5	0.96	2.55	3.316(4)	136.8
C(10)-H(10C)...Cl(1)#6	0.96	2.85	3.636(3)	139.3
C(10)-H(10C)...F(2)#7	0.96	2.51	3.193(4)	128.1

Symmetry transformations used to generate equivalent atoms:

#1  $-x, -y+1, -z+1$  #2  $x, -y+3/2, z+1/2$  #3  $x, -y+3/2, z-1/2$

#4  $-x+1, y+1/2, -z+3/2$  #5  $x, -y+1/2, z-1/2$  #6  $-x+1, -y+2, -z+1$

#7  $x, y+1, z$

## 16 Reference:

1. Dolomanov, O.V., Bourhis, L.J., Gildea, R.J., Howard, J.A.K., and Puschmann, H. (2009). OLEX2: a complete structure solution, refinement and analysis program. *J. Appl. Cryst.* 42, 339-341. doi:10.1107/S0021889808042726.

2. Sheldrick, G. (2015). SHELXT - Integrated space-group and crystal-structure determination. *Acta Cryst.* *A71*, 3-8. doi:10.1107/S2053273314026370.
3. Sheldrick, G. (2015). Crystal structure refinement with SHELXL. *Acta Cryst.* *C71*, 3-8. doi:10.1107/S2053229614024218.
4. Chen, S., Graceffa, R.F., and Boezio, A.A. (2016). Direct, Regioselective N-Alkylation of 1,3-Azoles. *Org. Lett.* *18*, 16-19. 10.1021/acs.orglett.5b02994.
5. Gottlieb, H.E., Kotlyar, V., and Nudelman, A. (1997). NMR Chemical Shifts of Common Laboratory Solvents as Trace Impurities. *The Journal of Organic Chemistry* *62*, 7512-7515. 10.1021/jo971176v.
6. Unger, E.L., Hoke, E.T., Bailie, C.D., Nguyen, W.H., Bowring, A.R., Heumüller, T., Christoforo, M.G., and McGehee, M.D. (2014). Hysteresis and transient behavior in current–voltage measurements of hybrid-perovskite absorber solar cells. *Energy & Environmental Science* *7*, 3690-3698. 10.1039/C4EE02465F.
7. Zhao, Y.-C., Zhou, W.-K., Zhou, X., Liu, K.-H., Yu, D.-P., and Zhao, Q. (2017). Quantification of light-enhanced ionic transport in lead iodide perovskite thin films and its solar cell applications. *Light Sci. Appl.* *6*, e16243-e16243. 10.1038/lsa.2016.243.
8. Chen, S., Ju, Y., Yang, Y., Xiang, F., Yao, Z., Zhang, H., Li, Y., Zhang, Y., Xiang, S., Chen, B., and Zhang, Z. (2024). Multistate structures in a hydrogen-bonded polycatenation non-covalent organic framework with diverse resistive switching behaviors. *Nat. Commun.* *15*, 298. 10.1038/s41467-023-44214-x.
9. Yu, J., Wang, H., Zhuge, F., Chen, Z., Hu, M., Xu, X., He, Y., Ma, Y., Miao, X., and Zhai, T. (2023). Simultaneously ultrafast and robust two-dimensional flash memory devices based on phase-engineered edge contacts. *Nat. Commun.* *14*, 5662. 10.1038/s41467-023-41363-x.
10. Zhao, Z., El-Khouly, M.E., Che, Q., Sun, F., Zhang, B., He, H., and Chen, Y. (2023). Redox-Active Azulene-based 2D Conjugated Covalent Organic Framework for Organic Memristors. *Angew. Chem. Int. Ed.* *62*, e202217249. <https://doi.org/10.1002/anie.202217249>.
11. Yan, X., Cao, G., Wang, J., Man, M., Zhao, J., Zhou, Z., Wang, H., Pei, Y., Wang, K., Gao, C., et al. (2020). Memristors based on multilayer graphene electrodes for implementing a low-power neuromorphic electronic synapse. *Journal of Materials Chemistry C* *8*, 4926-4933. 10.1039/D0TC00316F.
12. Zhang, M., Ma, C., Du, D., Xiang, J., Yao, S., Hu, E., Liu, S., Tong, Y., Wong, W.-Y., and Zhao, Q. (2020). Donor–Acceptor Metallopolymers Containing Ferrocene for Brain Inspired Memristive Devices. *Adv. Elect. Mat.* *6*, 2000841. <https://doi.org/10.1002/aelm.202000841>.
13. Albano, L.G.S., Vello, T.P., de Camargo, D.H.S., da Silva, R.M.L., Padilha, A.C.M., Fazzio, A., and Bufon, C.C.B. (2020). Ambipolar Resistive Switching in an Ultrathin Surface-Supported Metal–Organic Framework Vertical Heterojunction. *Nano Lett.* *20*, 1080-1088. 10.1021/acs.nanolett.9b04355.
14. Wang, K., Li, L., Zhao, R., Zhao, J., Zhou, Z., Wang, J., Wang, H., Tang, B., Lu, C., Lou, J., et al. (2020). A Pure 2H-MoS<sub>2</sub> Nanosheet-Based Memristor with Low Power Consumption and Linear Multilevel Storage for Artificial Synapse Emulator. *Adv. Elect. Mat.* *6*, 1901342. <https://doi.org/10.1002/aelm.201901342>.
15. Zhou, Z., Zhao, J., Chen, A.P., Pei, Y., Xiao, Z., Wang, G., Chen, J., Fu, G., and Yan, X. (2020). Designing carbon conductive filament memristor devices for memory and electronic synapse applications. *Materials Horizons* *7*, 1106-1114. 10.1039/C9MH01684H.
16. Yao, Z., Pan, L., Liu, L., Zhang, J., Lin, Q., Ye, Y., Zhang, Z., Xiang, S., and Chen, B. (2019). Simultaneous implementation of resistive switching and rectifying effects in a metal-

- organic framework with switched hydrogen bond pathway. *Sci. Adv.* *5*, eaaw4515. doi:10.1126/sciadv.aaw4515.
17. Liu, J., Yang, F., Cao, L., Li, B., Yuan, K., Lei, S., and Hu, W. (2019). A Robust Nonvolatile Resistive Memory Device Based on a Freestanding Ultrathin 2D Imine Polymer Film. *Adv. Mater.* *31*, 1902264. <https://doi.org/10.1002/adma.201902264>.
  18. Zhao, L., Wu, W., Shen, X., Liu, Q., He, Y., Song, K., Li, H., and Chen, Z. (2019). Nonvolatile Electrical Bistability Behaviors Observed in Au/Ag Nanoparticle-Embedded MOFs and Switching Mechanisms. *ACS Applied Materials & Interfaces* *11*, 47073-47082. 10.1021/acsami.9b17000.
  19. Ding, G., Wang, Y., Zhang, G., Zhou, K., Zeng, K., Li, Z., Zhou, Y., Zhang, C., Chen, X., and Han, S.-T. (2019). 2D Metal–Organic Framework Nanosheets with Time-Dependent and Multilevel Memristive Switching. *Adv. Funct. Mater.* *29*, 1806637. <https://doi.org/10.1002/adfm.201806637>.
  20. Yan, X., Wang, K., Zhao, J., Zhou, Z., Wang, H., Wang, J., Zhang, L., Li, X., Xiao, Z., Zhao, Q., et al. (2019). A New Memristor with 2D Ti3C2Tx MXene Flakes as an Artificial Bio-Synapse. *Small* *15*, 1900107. <https://doi.org/10.1002/smll.201900107>.
  21. Sokolov, A.S., Ali, M., Riaz, R., Abbas, Y., Ko, M.J., and Choi, C. (2019). Silver-Adapted Diffusive Memristor Based on Organic Nitrogen-Doped Graphene Oxide Quantum Dots (N-GOQDs) for Artificial Biosynapse Applications. *Adv. Funct. Mater.* *29*, 1807504. <https://doi.org/10.1002/adfm.201807504>.
  22. Yan, X., Zhang, L., Chen, H., Li, X., Wang, J., Liu, Q., Lu, C., Chen, J., Wu, H., and Zhou, P. (2018). Graphene Oxide Quantum Dots Based Memristors with Progressive Conduction Tuning for Artificial Synaptic Learning. *Adv. Funct. Mater.* *28*, 1803728. <https://doi.org/10.1002/adfm.201803728>.
  23. Yi, X., Yu, Z., Niu, X., Shang, J., Mao, G., Yin, T., Yang, H., Xue, W., Dhanapal, P., Qu, S., et al. (2019). Intrinsically Stretchable Resistive Switching Memory Enabled by Combining a Liquid Metal–Based Soft Electrode and a Metal–Organic Framework Insulator. *Adv. Elect. Mat.* *5*, 1800655. <https://doi.org/10.1002/aelm.201800655>.
  24. He, H.-K., Yang, R., Zhou, W., Huang, H.-M., Xiong, J., Gan, L., Zhai, T.-Y., and Guo, X. (2018). Photonic Potentiation and Electric Habituation in Ultrathin Memristive Synapses Based on Monolayer MoS<sub>2</sub>. *Small* *14*, 1800079. <https://doi.org/10.1002/smll.201800079>.
  25. Liu, B., Liu, Z., Chiu, I.-S., Di, M., Wu, Y., Wang, J.-C., Hou, T.-H., and Lai, C.-S. (2018). Programmable Synaptic Metaplasticity and below Femtojoule Spiking Energy Realized in Graphene-Based Neuromorphic Memristor. *ACS Applied Materials & Interfaces* *10*, 20237-20243. 10.1021/acsami.8b04685.
  26. Goswami, S., Matula, A.J., Rath, S.P., Hedström, S., Saha, S., Annamalai, M., Sengupta, D., Patra, A., Ghosh, S., Jani, H., et al. (2017). Robust resistive memory devices using solution-processable metal-coordinated azo aromatics. *Nat. Mater* *16*, 1216-1224. 10.1038/nmat5009.
  27. Liu, Y., Wang, H., Shi, W., Zhang, W., Yu, J., Chandran, B.K., Cui, C., Zhu, B., Liu, Z., Li, B., et al. (2016). Alcohol-Mediated Resistance-Switching Behavior in Metal–Organic Framework-Based Electronic Devices. *Angew. Chem. Int. Ed.* *55*, 8884-8888. <https://doi.org/10.1002/anie.201602499>.
  28. Pan, L., Ji, Z., Yi, X., Zhu, X., Chen, X., Shang, J., Liu, G., and Li, R.-W. (2015). Metal–Organic Framework Nanofilm for Mechanically Flexible Information Storage Applications. *Adv. Funct. Mater.* *25*, 2677-2685. <https://doi.org/10.1002/adfm.201500449>.
  29. Pan, L., Liu, G., Li, H., Meng, S., Han, L., Shang, J., Chen, B., Platero-Prats, A.E., Lu, W., Zou, X., and Li, R.-W. (2014). A Resistance-Switchable and Ferroelectric Metal–Organic Framework. *J. Am. Chem. Soc.* *136*, 17477-17483. 10.1021/ja508592f.

30. Huang, X., Zheng, B., Liu, Z., Tan, C., Liu, J., Chen, B., Li, H., Chen, J., Zhang, X., Fan, Z., et al. (2014). Coating Two-Dimensional Nanomaterials with Metal–Organic Frameworks. *ACS Nano* *8*, 8695-8701. 10.1021/nn503834u.
31. Yoon, S.M., Warren, S.C., and Grzybowski, B.A. (2014). Storage of Electrical Information in Metal–Organic-Framework Memristors. *Angew. Chem. Int. Ed.* *53*, 4437-4441. <https://doi.org/10.1002/anie.201309642>.
32. Sup Choi, M., Lee, G.-H., Yu, Y.-J., Lee, D.-Y., Hwan Lee, S., Kim, P., Hone, J., and Jong Yoo, W. (2013). Controlled charge trapping by molybdenum disulphide and graphene in ultrathin heterostructured memory devices. *Nat. Commun.* *4*, 1624. 10.1038/ncomms2652.
33. Zhu, X., Li, D., Liang, X., and Lu, W.D. (2019). Ionic modulation and ionic coupling effects in MoS<sub>2</sub> devices for neuromorphic computing. *Nat. Mater* *18*, 141-148. 10.1038/s41563-018-0248-5.